INTERNATIONAL JOURNAL FOR NUMERICAL METHODS IN FLUIDS, VOL. 9, 453–492 (1989)

A FINITE ELEMENT METHOD FOR ANALYSIS OF FLUID FLOW, HEAT TRANSFER AND FREE INTERFACES IN CZOCHRALSKI CRYSTAL GROWTH

P. A. SACKINGER AND R. A. BROWN

Department of Chemical Engineering and Materials Processing Center, Massachusetts Institute of Technology, Cambridge, MA 02139, U.S.A.

AND

J. J. DERBY

Lawrence Livermore National Laboratory, University of California, Livermore, CA 94550, U.S.A.

SUMMARY

A finite element algorithm is presented for simultaneous calculation of the steady state, axisymmetric flows and the crystal, melt/crystal and melt/ambient interface shapes in the Czochralski technique for crystal growth from the melt. The analysis is based on mixed Lagrangian finite element approximations to the velocity, temperature and pressure fields and isoparametric approximations to the interface shape. Galerkin's method is used to reduce the problem to a non-linear algebraic set, which is solved by Newton's method. Sample solutions are reported for the thermophysical properties appropriate for silicon, a low-Prandtl-number semiconductor, and for GGG, a high–Prandtl–number oxide material. The algorithm is capable of computing solutions for both materials at realistic values of the Grashof number, and the calculations are convergent with mesh refinement. Flow transitions and interface shapes are calculated as a function of increasing flow intensity and compared for the two material systems. The flow pattern near the melt/gas/crystal tri-junction has the asymptotic form predicted by an inertialess analysis assuming the meniscus and solidification interfaces are fixed.

KEY WORDS Czochralski crystal growth Finite element method Free boundary problem, Incompressible fluid flow Heat transfer

1. INTRODUCTION

The Czochralski (CZ) crystal growth technique is the most widely used method for producing large single crystals of silicon and many other semiconductor materials for use as substrates in the fabrication of electronic devices.[1–3] Many refractory oxide crystals which are used in the production of solid state lasers and optical devices are also produced by the CZ method.[4] A variant of the CZ process known as liquid–encapsulated Czochralski growth (LEC) is used for the growth of gallium arsenide (GaAs) and other compound semiconductors.[5] Here a layer of inert encapsulant, usually boric oxide (B_2O_3), is floated on the surface of the melt in order to prevent the loss of volatile components, like As in GaAs, from the melt.

In the CZ method a cylindrical single crystal is pulled vertically from the surface of a heated pool of melt contained in a cylindrical crucible, as shown schematically in Figure 1. Resistance

Received 12 February 1988
Revised 11 July 1988

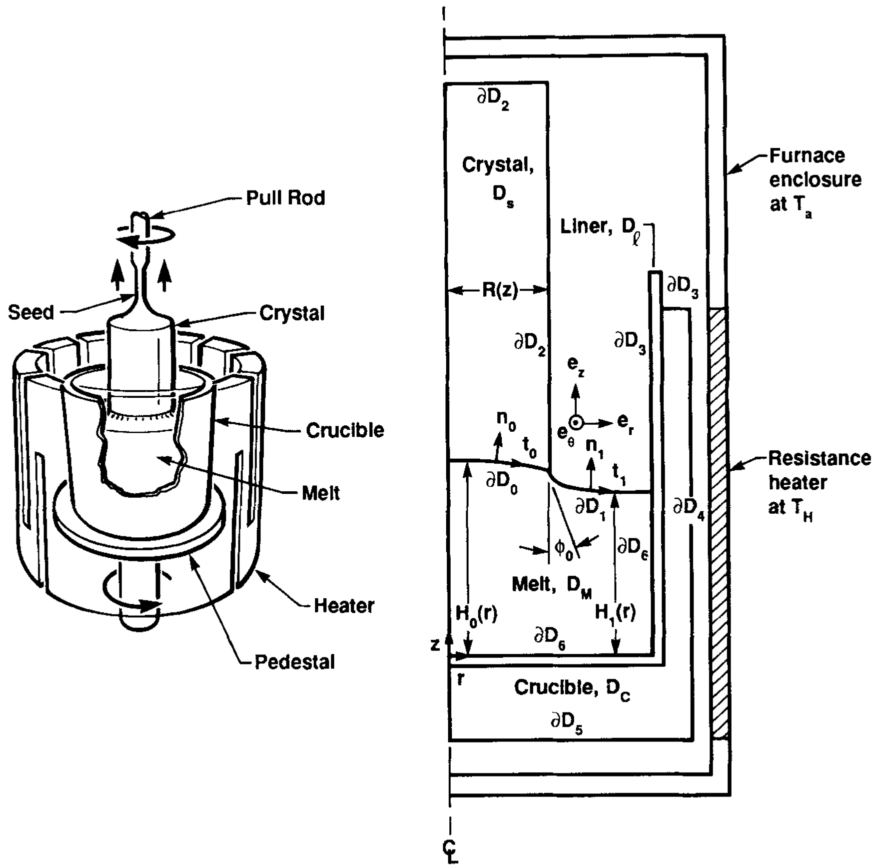

Figure 1. Schematic of the Czochralski crystal growth configuration showing domains for mathematical model and free surfaces

heating is typically used for semiconductor systems, and inductive heating is common for the higher-melting-point oxide materials. Growth is initiated by lowering a small seed crystal to the surface of the melt pool so that it connects to the melt pool along a melt/crystal interface which is joined at the edges by the melt/ambient meniscus. After thermal equilibration of the seed with the melt, the seed is raised and the temperature of the melt is lowered to induce growth of the crystal. By control of the thermal environment and other parameters, the crystal radius is increased to a desired value and then kept constant as the melt level drops.

The objective of the design and control of a CZ crystal growth system is the growth of a constant radius crystal with uniformly distributed solutes and impurities and a low number of defects in its crystallographic structure. The interactions of heat transfer, interfacial phenomena, hydrodynamics in the melt, and dopant transport that occur in Czochralski crystal growth all influence these objectives. These couplings are characteristic of the complexity of meniscus-defined solidification processes in which a single crystal is grown from the exposed surface of its melt. Because the high temperatures of typical CZ systems prevent the use of many types of sensors during crystal growth, large-scale numerical simulations of the transport processes in CZ and other crystal growth systems provide the only means for probing these complex couplings.

Numerical analysis of a self-consistent model for Czochralski growth requires solution of the complex free-boundary problem that defines the shape of the crystal, the melt/crystal interface, the meniscus and the field variables, i.e. the temperature in all phases and the velocity and pressure fields in the melt. We have referred to models that include the coupling of the interfaces to heat transfer as *thermal-capillary models* (or TCMs) of CZ growth.[1] The purpose of this paper is to present a finite element algorithm for solution of thermal-capillary models that include a detailed description of convection in the melt, a so-called *Hydrodynamic TCM* or *HTCM*.

Previous models for the CZ method have concentrated on analysis of either heat transfer and melt convection in idealized systems[6-10] or on heat transfer alone in conjunction with determination of the interfaces in the system;[11-14] see Reference 15 for a comprehensive review of this latter type of analysis. The discussion here focuses on studies in the first category, which were referred to as analysis of Czochralski 'bulk flow' by Langlois.[6]

The idealized geometry used in bulk flow analyses of hydrodynamics in Czochralski growth takes the melt/crystal and melt/ambient interfaces to be flat so that the melt is simply a cylinder with varying thermal and velocity boundary conditions about its edges. The radius of the crystal is set, and the temperature of the melt/crystal interface is specified at the melting point. Heat transport in the crystal is not computed, so the crystal radius appears as a parameter in the analysis. Heat input into the melt is usually characterized by a constant temperature for the crucible wall, so that the intensity of convection in the melt can be scaled with a Grashof number, $Gr^* \equiv g\beta_m R_{cruc}^3 \Delta T_m/\nu_m^2$, defined in terms of the radius of the crucible, R_{cruc}, and the temperature difference between the crucible wall and the melting point, ΔT_m. The majority of the calculations reported for this system have been for thermophysical properties characteristic of semiconductor materials, where the large thermal conductivity and small kinematic viscosity lead to a low Prandtl number ($\sim 0{\cdot}01$) in the melt. Oxide melts typically have Prandtl numbers in the range 1–10 or greater.

Kobayashi[7] first computed steady state, axisymmetric flow fields for low values of Gr^* and showed the effects of buoyancy-driven convection and crucible and crystal rotation on the viscous flow structure. Langlois[6], Mihelčic *et al.*[8] and Crochet *et al.*[9] have reported time-dependent calculations of axisymmetric flows. The results of Crochet *et al.* show clearly the development of time-periodic motion in low–Prandtl–number melts as Gr^* is increased. The oscillations begin as a Hopf bifurcation from the steady state motion after separation of the flow from the vertical wall of the crucible. The separated flow becomes unstable as the intensity is increased by a mechanism involving the dynamic interaction of the multiple flow cells created by the separation. For the idealized geometry, a specific melt volume and a Prandtl number in the melt $Pr = 0{\cdot}015$, the onset of the oscillations occurred at $Gr^* = O(10^6)$. These oscillatory motions are unwanted because they lead to periodic melting and resolidification of the crystal and to fluctuations in the composition of the crystal.[1]

Although the results of the analyses of CZ bulk flow have elucidated many of the features of the convection in the melt, the results cannot be applied directly to experimental systems since the analyses ignored the interactions between heat transfer and convection in the melt with the size and shape of melt and the crystal. The analysis described here includes the free boundaries for the CZ system; the crystal shape, the melt/crystal interface and the meniscus.

We build on the finite element analysis described by Derby *et al.*[12] for solution of thermal–capillary models of CZ growth, which included the interactions of the free boundaries with conductive heat transfer in all phases but neglected convection in the melt. The analysis is based on deforming, isoparametric Lagrangian finite elements for representing field variables in all phases *and* the interface shapes separating the phases. The non-linear coupling of the finite element basis functions to the location of the element nodes intertwines the calculation of the field variables and the interface shapes. A mixed Lagrangian basis set that is convergent for the Boussinesq equations is used, and the partial differential equations are discretized using Galerkin's method.

Independent sets of residual equations are distinguished to represent the shape of each interface. The normal stress balance is used for locating the meniscus. This is an extension of the method in Reference 12 to include the effects of normal viscous forces and dynamic pressure and is similar to the method first implemented by Silliman and Scriven[16] (also see Kistler and Scriven[17]) to solve viscous free surface flows. This formulation reduces to the Young–Laplace equation for a static meniscus shape and to the formulation of Derby *et al.*[12] when hydrodynamic interactions are unimportant. Distinguishing the normal stress balance for determining the shape of the melt/gas meniscus runs in parallel to the analysis of Bemelmans[18] for formal proof of existence of viscous flow problems with a capillary surface.

The isotherm condition is used as the distinguished condition for the melt/crystal interface. Ettouney and Brown[19] show that this choice leads to interface shapes computed to the same order of accuracy as the temperature field. This formulation has been incorporated into solidification problems including convection in the melt,[20,21] In the quasi-steady state formulation considered here, the crystal must be a cylinder with radius determined so that a wetting angle condition at the melt/crystal/gas tri-junction is satisfied. Following the formulation for the conduction-dominated model,[12] we use this condition to determine the radius of the crystal.

The coupled set of residual equations is solved by Newton's method, with the Jacobian matrix formed by explicit differentiation of each residual equation with respect to both field variables and interface shapes. As Ruschak[22] and others[12,20,23,24] have demonstrated, the added complexity of formulating the Jacobian matrix and the direct solution of the linear equation set is more than offset by the rapid convergence and robustness of the Newton iterations for the coupled set. These features are essential for the CZ problem, where any successive iteration technique must account for three free boundaries.

The presence of the melt/crystal/gas tri-junction introduces the possiblity of a singularity in the flow field at this point; this singularity has been termed a static contact point.[25] Local asymptotic analysis has been used to study the form of the flow in the neighbourhood of discontinuities in the boundary data. In the limit where the meniscus has a set shape and inertia is unimportant, the separation of variables solution used by Dean and Montagnon[26] and by Moffatt[27] describes the form of the flow near the singularity. The results of this approach are reproduced in Section 2.4 to predict the degree of the singularity in the flow field at the tri-junction as a function of separation angle between the melt/crystal interface and the melt/gas meniscus. For the range of separation angles encountered in this meniscus-defined crystal growth system, the combination of no-slip and shear-free boundary conditions at the melt/crystal interface and melt/gas meniscus results in a singularity that is not too severe; the stress remains integrable.

The validity of the asymptotic analysis of Moffatt[27] for a meniscus shape that interacts with the flow field is an open question. Silliman and Scriven[16] suggested that the fluid must be allowed to slip along the solid boundary—in this case the melt/crystal interface—to obtain an integrable stress and tested this idea on calculations of extrudate swell. The regular perturbation analysis of Trogdon and Joseph[28] for small capillary number, a measure of the importance of normal viscous forces relative to surface tension, suggests that the separable solution has some range of validity in this limit. We pursue this approach here.

The calculations described here are based on a simple model of radiative heat transport in which all surfaces in the CZ system view black bodies of fixed temperature but do not view each other. Atherton *et al.*[14] (see also Reference 13) have extended the TCM to include diffuse-grey radiative exchange between interacting surfaces, such as the melt, crystal and crucible. This analysis extends to the HTCM, as described in Reference 29.

We present solutions for CZ growth of both semiconductor silicon and the oxide gadolinium gallium garnet ($Gd_3Ga_5O_{12}$), hereafter referred to as GGG, to contrast the development of the flow structure for low- and high-Prandtl-number melts. The calculations in Sections 4 and 5 are confined to analysis of buoyancy-driven flows and to the accuracy of the finite element calculations for two systems. A more extensive analysis including the flows driven by rotation of the crucible and crystal, thermocapillary driven flows and effects of an external magnetic field will be presented elsewhere.

2. FORMULATION

2.1. Field equations

The physical configuration of the mathematical model for CZ growth is shown schematically in Figure 1. The multiple domains represent different physical regions of the system: crystal (*s*), melt (*m*), crucible (*c*) and crucible liner (*l*), each of which is characterized by different thermophysical properties. The cylindrical co-ordinate system (r, z, θ) is centred at the bottom of the crucible, and the unknown boundary shapes are represented by the functions $H_0(r)$ and $H_1(r)$ for the melt/crystal interface and the melt meniscus respectively and by $R(z)$ for the shape of the crystal. In this quasi-steady state analysis $R(z)$ has a constant value, so that a cylindrical crystal shape is assumed; however, its value is not set *a priori* but is calculated as part of the solution. This aspect is addressed in more detail below.

The quasi-steady state (QSS) approximation is used to derived the HTCM. In it the effects of the batchwise decrease of the melt volume and the evolving crystal radius are neglected. The operation of the system throughout the batch is simulated by a sequence of steady state calculations at different values of the melt volume. Derby and Brown[30] assessed the validity of the QSS approximation and found it to be accurate for long crystals in systems with good radius control.

The thermal-capillary model (TCM) originally put forth by Derby *et al.*[12] accounts for conductive heat transfer in each domain, with an additional convective term in the crystal to account for its upward velocity as it is slowly pulled from the melt. We retain this model for heat transport in the crystal, crucible and liner. The energy equations for these phases are written in dimensionless form as

$$Pe_s \frac{\partial T}{\partial z} = \nabla \cdot (K_s \nabla T), \tag{1}$$

$$0 = \nabla \cdot (K_c \nabla T), \tag{2}$$

$$0 = \nabla \cdot (K_l \nabla T), \tag{3}$$

where Pe_s is the Peclet number for heat transfer in the crystal and K_i, $i = \mathrm{s, c, l}$, are reduced thermal conductivities of each phase (scaled with the reference value of the conductivity of the crystal at the melting temperature) which are allowed to be functions of temperature. The temperature has been scaled with the absolute melting point temperature T_{mp}, and the lengths with $L = R_{cruc}$, the inner radius of the crucible/liner assembly. A complete listing of dimensionless groups is given in Table I.

The extension of the TCM to include fluid flow requires the modification of the energy equation in the melt and introduces additional field equations for the velocity and pressure in the melt. The

Table I. Dimensionless groups appearing in the HTCM

Symbol	Definition	Name/description
Bo	$\rho_m g L^2/\gamma$	Bond no.; g is the gravitational constant
Bi_j	$h_j L/k_s$	Biot no. for heat transfer at surface j
Ca	$\mu_m \alpha_m/\gamma L$	Capillary no.
Gr	$g\beta_m T_{mp} L^3/\nu_m^2$	Grashof no. in melt, based on absolute melting point temperature
Gr^*	$Gr \Delta T_m/T_{mp}$	Grashof no. in melt, based on temperature difference in melt
Ma	$(d\gamma/dT) T_{mp} L/\alpha_m \mu_m$	Marangoni no. based on absolute melting point temperature
Pe_s	$V_g L/\alpha_s$	Peclet no. for heat transfer in crystal
Pe^*	$V^* L/\alpha_m$	Peclet no. for heat transfer in melt, based on maximum velocity in melt
Pr	ν_m/α_m	Prandtl no.
Rd_j	$\varepsilon_j \sigma_{(SB)} T_{mp}^3 L/k_s$	Radiation no. for heat transfer from surface j; $\sigma_{(SB)}$ is the Stefan–Boltzmann constant
Re_c	$\omega_c L^2/\nu_m$	Rotational Reynold's no. for crucible
Re_s	$\omega_s L^2/\nu_m$	Rotational Reynold's no. for crystal based on crucible radius
Re_s^*	$\omega_s R^2/\nu_m$	Rotational Reynold's no. for crystal based on crystal radius
Re^*	$V^* L/\nu_m$	Reynolds no. in melt, based on maximum velocity in melt
S	$\Delta H_f/C_{pm} T_{mp}$	Stefan no.
We	$\rho_m \alpha_m^2/\gamma L$	Weber no.

momentum and continuity equations are written in dimensionless form using the Boussinesq approximation:

$$\mathbf{v}\cdot\nabla\mathbf{v} = \nabla\cdot\boldsymbol{\sigma} + Gr Pr^2 (T-1)\mathbf{e}_z, \tag{4}$$

$$K_m \mathbf{v}\cdot\nabla T = \nabla\cdot(K_m \nabla T), \tag{5}$$

$$\nabla\cdot\mathbf{v} = 0, \tag{6}$$

where Gr is the Grashof number, Pr is the Prandtl number and $K_m = k_m/k_s$ is the ratio of the thermal conductivity of the melt to the thermal conductivity of the crystal. The velocity has been made dimensionless using the thermal scaling α_m/L, where α_m is the thermal diffusivity of the melt. See Table I for the definitions of Gr and Pr.

The dimensionless stress tensor $\boldsymbol{\sigma}$ is given in terms of P, the deviation of the pressure from the hydrostatic value, and the deviatoric stress $\boldsymbol{\tau}$ as

$$\boldsymbol{\sigma} = -P\mathbf{I} + \boldsymbol{\tau}, \tag{7}$$

where the deviatoric stress for a Newtonian fluid is

$$\boldsymbol{\tau} = Pr(\nabla\mathbf{v} + \nabla\mathbf{v}^T).$$

Both P and $\boldsymbol{\tau}$ have been scaled with the viscous reference $\mu_m \alpha_m/L^2$, where μ_m is the viscosity of the melt. Writing the momentum equation in terms of the stress tensor facilitates the application of boundary conditions at the melt/gas interface in the finite element formulation of the model.

The Grashof number appearing in (4) is defined using the temperature scale T_{mp} (see Table I.) The value of Gr defined in this way does not provide a useful measure of the driving force for natural convection; in fact, Gr will be a constant dependent only on the thermophysical properties of the melt and thus is insensitive to the operating conditions. A better basis for comparison with other studies of convection in idealized models is obtained by defining Gr^* as

$$Gr^* \equiv Gr \frac{\Delta T_{\mathrm{m}}}{T_{\mathrm{mp}}}, \tag{8}$$

where ΔT_{m} is the maximum temperature difference in the melt, i.e.

$$\Delta T_{\mathrm{m}} = \max_{D_{\mathrm{m}}} T - \min_{D_{\mathrm{m}}} T = \max_{D_{\mathrm{m}}} T - T_{\mathrm{mp}}, \tag{9}$$

where D_{m} denotes the melt. Because of the interrelationship between heat transfer in all of the phases, ΔT_{m} is not known *a priori*. Instead, Gr^* is computed after solving the HTCM. Unless there is undercooling, the minimum temperature in the melt will be T_{mp} at the melt/crystal interface; the maximum temperature will occur along the inner sidewall of the crucible linear where heat enters the melt.

2.2. Boundary conditions

An outstanding feature of the TCM is that it incorporates the free boundaries inherent to the CZ system with the heat transfer calculation. The shapes of the melt/solid interface, melt/gas interface and crystal are determined simultaneously with the temperature field throughout the system. The HTCM adds the effects of dynamic pressure and viscous stress on the shape of the melt/gas interface. The fluid flow interacts only indirectly with the shape of the melt/crystal interface and crystal radius insofar as the convection affects the temperature field.

At the melt/crystal interface (∂D_0) latent heat is generated as a result of solidification as the crystal is pulled upwards. The energy balance along this interface is

$$\mathbf{n}_0 \cdot (K_{\mathrm{m}} \nabla T - K_{\mathrm{s}} \nabla T) = Pe_{\mathrm{s}} S \mathbf{n}_0 \cdot \mathbf{e}_z, \tag{10}$$

where $\mathbf{n}_0$ is the unit normal vector to the melt/solid interface and S is the Stefan number. The product $Pe_{\mathrm{s}}S$ is a measure of the relative importancee of latent heat generation due to solidification and conductive heat transfer. Again, since the temperature is scaled with T_{mp}, the definition of the Stefan number S depends on material properties and not on the operating conditions. An idealization embedded in (10) is that the growth rate of the crystal is identical with the pull rate, an assumption which is valid only if the melt height is constant. A 'batch correction' based on a simple mass balance to account for this effect is given in Reference 30 and is included in the model discussed in Reference 29.

Thermal boundary conditions are applied at the exposed surfaces of the system which describe both radiative and convective contributions to the heat flux. The radiative transfer is written for an idealized situation in which each surface views a specified ambient temperature. This temperature boundary condition is

$$K_i \mathbf{n}_j \cdot \nabla T = Bi_j (T - T_{\mathrm{a}}(r, z)) + Rd_j (T^4 - T_{\mathrm{a}}^4(r, z)), \tag{11}$$

where i and j are used to denote the particular domains and surfaces respectively and Bi_j and Rd_j are the Biot and radiation numbers which scale the heat transfer at the surface due to convective cooling by the gas and radiative energy loss, respectively. A more realistic calculation of radiative heat transfer between the surface elements and the ambient for the TCM is described in Reference 14 and its implementation in the HTCM is detailed in Reference 29.

For all surfaces except the outer crucible wall, $T_a(r, z)$ is set to a lower temperature than the system so that cooling occurs from these surfaces. For the outer wall (∂D_4), $T_a(r, z)$ is set to the temperature of the heater, T_H. This representation is valid for describing a crucible heated radiatively by a separate resistive element as depicted in Figure 1 for silicon growth, but is an idealization for inductive heating systems commonly used for oxide growth. An analysis of the inductive heating of a CZ crucible is described in Reference 31 and its incorporation into the HTCM is presented in Reference 29.

The kinetics of solidification are assumed to be sufficiently fast so that the melt/solid phase boundary is at the equilibrium melting point. Then

$$T(r, z)|_{z=H_0(r)} = 1 \tag{12}$$

is the isotherm condition in the dimensionless form.

At the melt/gas interface the normal component of stress is set to balance the capillary pressure difference caused by surface tension. In dimensionless form this equation is

$$2\mathscr{H} = Bo(H_1(r) + \lambda) - We\mathbf{n}_1\mathbf{n}_1 : \boldsymbol{\sigma}, \tag{13}$$

where $2\mathscr{H}$ is the mean curvature of the interface, given in terms of $H_1(r)$ as

$$2\mathscr{H} = \frac{H_1''}{(1+(H_1')^2)^{3/2}} + \frac{H_1'}{r(1+(H_1')^2)^{1/2}},$$

where $H_1' \equiv \mathrm{d}H_1/\mathrm{d}r$, and $\mathbf{n}_1$ is the unit normal to the meniscus. The hydrodynamic contribution to the normal stress balance is multiplied by the Weber number We. Examining the individual terms that comprise the normal stress shows that the pressure term in (7) is multiplied by We, the ratio of inertial forces to surface tension, and the dimensionless deviatoric stress term $(\nabla\mathbf{v} + \nabla\mathbf{v}^T)$, is multiplied by the capillary number $Ca \equiv WePr$, the ratio of normal viscous forces to surface tension.

The bond number Bo, defined in Table I, is present in the conduction-dominated TCM and scales the effect of gravity on the shape of the meniscus. The reference pressure difference λ also appears in the basic TCM and serves as a Lagrange multiplier, determined from the constraint of a constant volume melt. Within the framework of the QSS assumption the dimensionless melt volume V_m, is

$$\frac{V_m}{2\pi} = \int_0^R H_0(r) r\,\mathrm{d}r + \int_R^1 H_1(r) r\,\mathrm{d}r, \tag{14}$$

where R is the crystal radius. The constant V_m is chosen to correspond to a particular stage of the crystal growth process.

The dimensionless crystal radius R that appears in (14) is also an unknown. The corresponding boundary condition associated with R is an equilibrium growth angle ϕ_0 which determines the slope of the meniscus at the growth tri-junction (see Figure 1):

$$\left.\frac{\mathrm{d}H_1}{\mathrm{d}r}\right|_{r=R} = -\cot\phi_0. \tag{15}$$

Similarly, at $r = 1$, a wetting angle is specified where the melt/gas interface meets the crucible wall. We assume that the melt does not wet the crucible ($\phi_0 = 90°$) so the derivative of H_1 vanishes:

$$\left.\frac{\mathrm{d}H_1}{\mathrm{d}r}\right|_{r=1} = 0. \tag{16}$$

At the growth tri-junction the interface shapes $H_0(r)$ and $H_1(r)$ meet, i.e.

$$H_0(R) = H_1(R). \tag{17}$$

Boundary conditions on temperature and velocity at the centreline ($r=0$) follow from the assumed axial symmetry of the solution:

$$\frac{\partial T}{\partial r} = \frac{\partial v_z}{\partial r} = 0, \qquad r=0 \tag{18}$$

and

$$v_r = v_\theta = 0, \qquad r=0. \tag{19}$$

While the temperature is continuous from the melt into the adjoining liner and crucible, the field equations for velocity apply only in the melt, and boundary conditions for **v** must be specified on the surfaces ∂D_0, ∂D_1 and ∂D_6 denoted in Figure 1.

At the melt/crystal interface (∂D_0) the velocity field must satisfy the no-slip boundary condition:

$$v_r = v_z = 0, \qquad v_\theta = Re_s Pr\, r, \tag{20}$$

where Re_s is a Reynolds number for rotational motion of the crystal, defined using L as a length scale. A second rotational Reynolds number for the crystal is defined using the crystal radius, which, generally is unknown *a priori*:

$$Re_s^* = Re_s = \frac{R}{L}. \tag{21}$$

Note that, consistent with the QSS assumption, the normal component of velocity at ∂D_0 due to solidfication is ignored. Including the solidification rate poses a dilemma for a QSS model. Since the melt volume contains an incompressible fluid, any mass leaving the system must be compensated for by an equivalent influx of mass, as is the case for continuous melt replenishment. A fully dynamical HTCM would account for mass leaving the system due to solidification by a decrease in the height of the melt/crystal and melt/gas interfaces. This velocity will typically be several orders of magnitude smaller than other characteristic fluid velocities in the system due to buoyancy, rotation, etc.[30]

The no-slip boundary condition is imposed where the melt meets the crucible linear (∂D_6) as

$$v_r = v_z = 0, \tag{22}$$

$$v_\theta = Re_c Pr\, r, \tag{23}$$

where Re_c is a Reynolds number for the rotational motion of the crucible.

No fluid crosses the melt/gas interface (∂D_1), and at steady state the boundary condition on the normal component of velocity is simply

$$\mathbf{v}\cdot\mathbf{n}_1 = 0. \tag{24}$$

Boundary conditions on the tangential stress are applied at ∂D_1 and are written in terms of two tangent vectors ($\mathbf{e}_\theta$, $\mathbf{t}_1$) on this surface (see Figure 1). From the assumption of axial symmetry the azimuthal component of the tangential stress balance is trivial:

$$\mathbf{e}_\theta \mathbf{n}_1 : \boldsymbol{\sigma} = 0, \tag{25}$$

while the component in the meridional direction ($\mathbf{t}_1$) includes tangential stress generated by surface tension gradients:

$$\mathbf{t}_1\mathbf{n}_1:\boldsymbol{\sigma} = -MaPr\frac{1}{\sqrt{(1+H_1'^2)}}\frac{\partial T}{\partial r}, \tag{26}$$

where the Marangoni number Ma is defined in Table I.

2.3. *Radius control*

The QSS model formulated above treats the crystal radius as an unknown which is determined as part of the solution to the field equations and boundary conditions. The crystal radius is sensitive to the operating environment and to the relative importance of convective heat transfer. The desire to grow crystals with constant radius has led to the extensive development of algorithms for automatic control during the batchwise growth process.

The model presented here is modified to analyse growth at a constant crystal radius by a method first put forth in Reference 32. In particular, the radius is set to the desired value and an augmented equation is used to find the heater temperature consistent with the given crystal radius $R = R_{\text{set}}$. The corresponding augmented equation is

$$0 = R - R_{\text{set}}, \tag{27}$$

where the heater temperature T_{H} becomes the additional unknown and appears in the flux boundary condition for the outside surface of the crucible (∂D_4), where $T_{\text{a}}(r, z)$ in (11) is replaced by T_{H}.

2.4. *Analysis of tri-junction singularity*

The junction of the melt, crystal and ambient leads to discontinuities in the boundary conditions for momentum transport and to a sharp corner in the flow domain. These differences may lead to singularities in the flow field and possibly to non-integrable forces along the solid boundaries, as has been documented for moving contact lines.[25] In this section we present a simple analysis to determine the form of the flow field near the melt/crystal/gas tri-junction for several combinations of boundary conditions along the melt/crystal and melt/gas interfaces. The analysis described here is taken from the more general treatment of singularities in Stokes flows presented by Moffatt[27] and the earlier work of Dean and Montagnon.[26]

We assume that the character of the flow near the tri-junction is recovered by analysis of a small inertialess region sufficiently close to the corner that the melt/crystal and melt/gas interfaces are approximately planar and are unaffected by the flow. These are good approximations when the thermal Peclet number is small in this region and when $We \ll 1$, as it is for semicondutor and oxide melts. This geometry is shown in Figure 2 along with the cylindrical polar co-ordinates (ρ, ϑ) used to represent the flow near the singularity.

Following Moffatt[27] we take the streamfunction as

$$\Psi(\rho, \vartheta) = \rho^{\lambda} f_{\lambda}(\vartheta). \tag{28}$$

The constant λ is the eigenvalue with smallest real part determined from the problem formed by inserting equation (28) into the momentum equation written in the local polar co-ordinate system and imposing the no-penetration condition and either the no-slip or shear-free condition on the two segments of the boundary. Because λ is generally complex, we write $\lambda = \lambda_{\text{r}} + \text{i}\lambda_{\text{i}}$, where ($\lambda_{\text{r}}$, λ_{i}) are real and $\text{i} = \sqrt{-1}$.

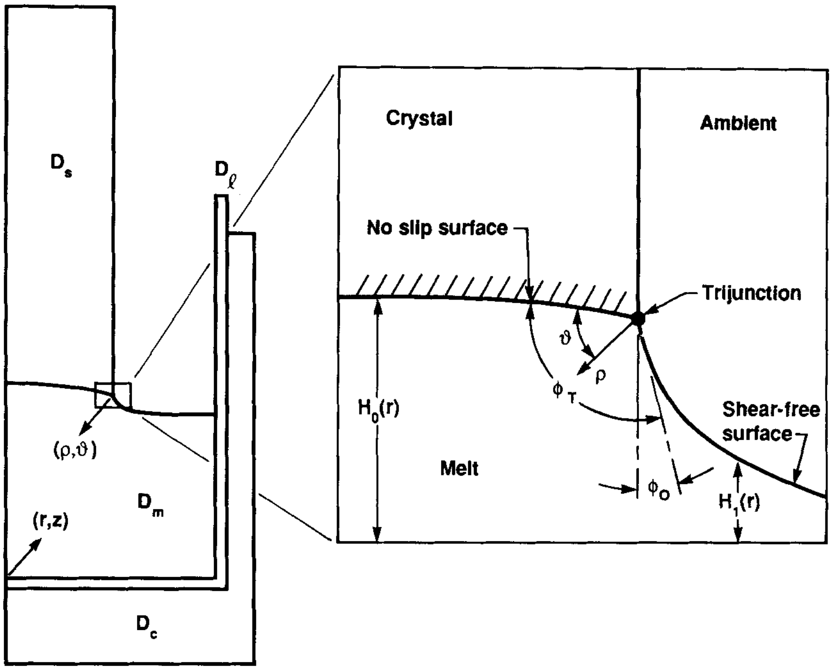

Figure 2. Schematic showing the melt/crystal/ambient tri-junction for the CZ system and the local polar co-ordinate system (ρ, ϑ)

The definition of the stream function, the equation of motion and the form of the stress tensor indicate that the pressure P and the components of the deviatoric stress τ scale as $\rho^{\lambda-2}$ as the singularity is approached ($\rho \rightarrow 0$). Therefore the components of the stress are singular whenever $\lambda_r < 2$ (except for the trivial case of $\lambda_r = 1$). Physically, the components of the stress should be square integrable, i.e. $\sigma_{ij} \in L^2(D_m)$. The separable form of (28) gives a direct interpretation between the real part of the Moffatt exponent and the square integrability of the stress σ_{ij}. Along a ray $\vartheta = \vartheta_0$ this requires

$$\left(\int_0^\infty |\sigma_{ij}(\rho, \vartheta_0)|^2 \, d\rho \right)^{1/2} < \infty, \tag{29}$$

which is satisfied only if $\lambda_r > 1{\cdot}5$ or $\lambda_r = 1$. The condition that the components of τ and the pressure are separately in $L^2(D_m)$ is also necessary for the solvability of the weak form of the momentum and continuity equations used in the finite element formulation. This formulation requires P and the gradients of $\mathbf{v}$ to be in $L^2(D_m)$.[33] These conditions are met if $\sigma_{ij} \in L^2(D_m)$.

The real part of the most dominant eigenvalue (λ_r) determined from this analysis is plotted in Figure 3 as a function of the separation angle ϕ_T at the tri-junction for two sets of boundary conditions. This separation angle depends on the slope of the melt/solid interface at the tri-junction and on the equilibrium growth angle ϕ_0 as

$$\phi_T = \phi_0 + 90^\circ - \tan^{-1}\left(\left. \frac{dH_0}{dr} \right|_{r=1} \right). \tag{30}$$

The combination of no-slip/shear-free (ns/sf) is appropriate for modelling conventional CZ growth. Note that the components of the stress become singular at $\phi_T \approx 128^\circ$, where $\lambda_r = 2$. The

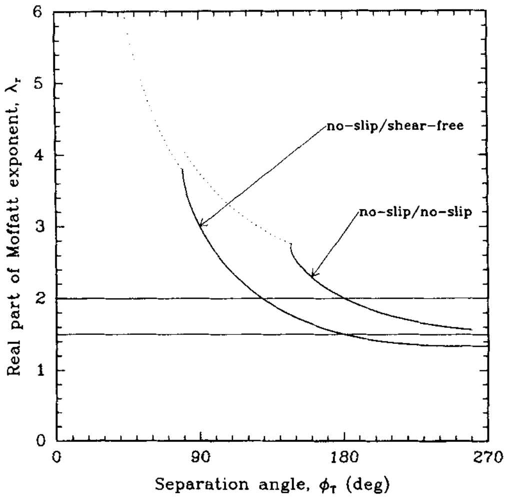

Figure 3. Results of asymptotic analysis for λ_r as a function of separation angle ϕ_T for ns/sf and ns/ns boundary conditions. Dotted curves indicate $\lambda_i \neq 0$

singularity becomes more severe with increasing ϕ_T, but remains integrable until $\phi_T = 180°$ ($\lambda_r = 1{\cdot}5$), reaching the limit for square integrable stresses and pressure. This analysis suggests that a flat meniscus as used in the bulk flow models for CZ growth gives the strongest singularity and is the most difficult in which to reproduce accurate local approximations to the solution. Also, the small wetting angles ($\phi_0 \sim 10°$–$20°$) which are characteristic of real melt/crystal/gas tri-junctions do not lead to singular stresses at all.

Forcing the velocity field to satisfy a no-slip condition (ns/ns) at the melt/gas interface makes the singularity less severe. As is well known, the stress is not singular at the corner unless the angle is re-entrant, i.e. $\phi_T > 180°$. For lower values of the separation angle, the dominant eigenvalue has an non-zero imaginary part, indicating the presence of an infinite sequence of viscous eddies in the corner near the tri-junction. The amplitude of these eddies is strongly damped as $\rho \to 0$, since $\lambda_r > 2{\cdot}5$ for both the ns/ns and the ns/sf cases when ϕ_T is in this regime. This sequence of eddies will exist in CZ systems when the crystal radius is decreasing as a function of time, i.e. where the effective growth angle measured from the vertical is less than zero, or if the melt/crystal interface is highly deflected near the tri-junction.

3. NUMERICAL METHOD

The non-linear coupling caused by the interactions of the interface shapes with energy and momentum transport make it extremely important that the algorithms for numerical solution of this problem explicitly account for the unknown interface shapes. The finite element approximations presented in Section 3.1 accomplish this. The Newton iteration scheme presented in Section 3.2 is a robust technique for simultaneous solution of the coupled set of algebraic equations.

3.1. *Finite element analysis*

The problem defined by (1)–(27) is reduced to a set of residual equations by approximating the velocity field, temperature field and interface shapes by expansions expressed in terms of finite element basis functions and unknown coefficients. A mesh is formed of quadrilateral elements which span the domains corresponding to the melt (D_m), crystal (D_s), crucible (D_c) and liner (D_l). Each interface (∂D_i) is defined by one-dimensional edges of the quadrilateral elements, so that the shape of the mesh is coupled to the solution of the field equations through the definition of the basis function. Sample meshes are shown in Figures 4 and 5. Finer discretizations are used near the boundaries of the melt to resolve the boundary layers in temperature and velocity which are expected there.

The field equations and boundary conditions are discretized using a mixed finite element basis set and Galerkin's method. The temperature field in all phases and the velocity in the melt are approximated by nine-node Lagrangian biquadratic polynomials $\{\Phi^i(r, z)\}$ as

$$\mathbf{v}(r, z) = \sum_{i=1}^{N_m} \begin{bmatrix} v_r^{(i)}\mathbf{e}_r \\ v_z^{(i)}\mathbf{e}_z \\ v_\theta^{(i)}\mathbf{e}_\theta \end{bmatrix} \Phi^i(r, z), \tag{31}$$

$$T(r, z) = \sum_{i=1}^{N} T^{(i)}\Phi^i(r, z), \tag{32}$$

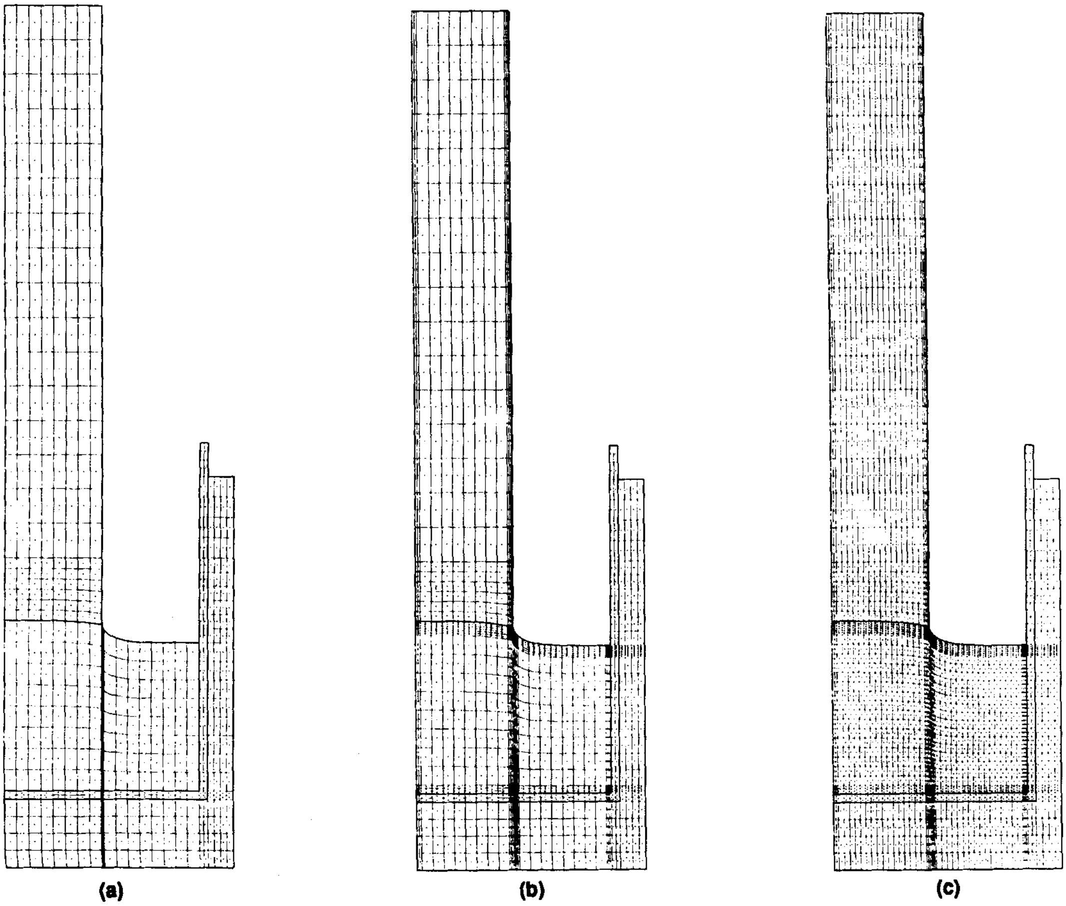

Figure 4. Finite element meshes used in convergence studies of the HTCM for Si; mesh (total number of unknowns) (a) M3 (6647), (b) M4 (13 999), (c) M5 (28 287)

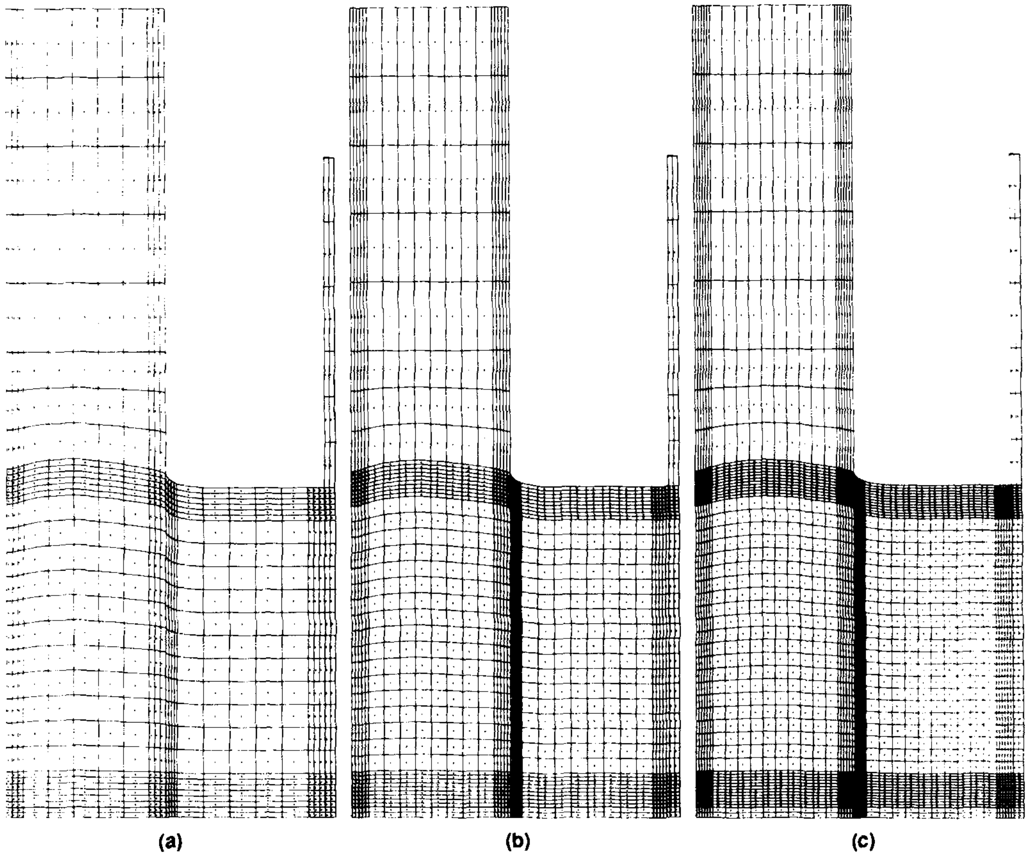

Figure 5. Finite element meshes used in convergence studies of the HTCM for GGG; mesh (total number of unknowns) (a) N1 (12042), (b) N2 (20928), (c) N3 (44079)

where N_m is the number of nodes in the melt and N is the total number of nodes in all phases. The isoparametric mapping consistent with the Lagrangian biquadratic basis is used to transform each element in the cylindrical co-ordinate system (r, z) to the co-ordinate system (ξ, η) where the element is square $(-1 \le \xi \le 1,\ -1 \le \eta \le 1)$. These two co-ordinate systems are related by

$$r = \sum_{i=1}^{9} r_i \phi^i(\xi, \eta), \qquad z = \sum_{i=1}^{9} z_i \phi^i(\xi, \eta), \tag{33}$$

where the global co-ordinates of each node are (r_i, z_i) and the biquadratic Lagrangian basis functions defined in terms of (ξ, η) are $\{\phi^i(\xi, \eta)\}$.[33]

The dynamic pressure in the melt is approximated by linear basis functions $\{\psi^i\}$ relative to the centroid node of each element in the transformed co-ordinate system. The pressure is represented as

$$P(r, z) = \sum_{i=1}^{N_p} P^{(i)} \psi^i(\xi(r, z), \eta(r, z)), \tag{34}$$

where N_p is the total number of pressure unknowns in the melt. The three linear basis functions $\{\psi^{[i]}\}$ within each fluid element are

$$\psi^{[1]}(\xi, \eta)=1, \qquad \psi^{[2]}(\xi, \eta)=\xi, \qquad \psi^{[3]}(\xi, \eta)=\eta,$$

where the superscript $[i]$ denotes a local numbering index; the mapping (33) transforms between the co-ordinate systems. This approximation to the pressure field is discontinuous between elements and yields an exact mass balance over each element.

The shapes of the melt/crystal interface and the melt meniscus are approximated by one-dimensional, three-node quadratic Lagrangian polynomials $\{\Gamma^i(r)\}$ which are consistent with the biquadratic interpolants and the isoparametric mapping used for the temperature and velocity fields. The ith interface shape is expressed as

$$H_i(r)=\sum_{j=1}^{N_i} H_i^{(j)}\Gamma^j(r), \tag{35}$$

where N_i is the number of nodes which fall along the ith interface.

The field equations are transformed into weak form by Galerkin's method. We implement the heat flux boundary conditions at the solidification interface, (10), and at the external boundaries, (11), as natural conditions in the weak form. The residual equations associated with the energy balances become

$$\begin{aligned}-\int_{D_j} K_j\nabla\Phi^i\cdot\nabla T\,\mathrm{d}V-\int_{D_s} Pe_s\Phi^i(\partial T/\partial z)\,\mathrm{d}V-\int_{D_m}\Phi^i\mathbf{v}\cdot\nabla T\,\mathrm{d}V+\int_{\partial D_0} Pe_s S\Phi^i(\mathbf{n}_0\cdot\mathbf{e}_z)\,\mathrm{d}S\\ -\int_{\partial D_k}\Phi^i[Bi_k(T-T_a)+Rd_k(T^4-T_a^4)]\,\mathrm{d}S=0,\end{aligned} \tag{36}$$

where $i=1, \ldots, N$ represents the residual equation for each node, $j=$ m, s, c, l represents each of the mesh regions and $k=1, \ldots, 5$ denotes the bounding external surfaces. Nine-point Gaussian quadrature is used to calculate all area integrals and three-point quadrature for all line integrals.

The isotherm condition for the temperature at the melt/crystal interface, (12), is formulated as a residual equation for determining the location of this interface:

$$\int_0^R \Gamma^i[T(r, H_0(r))-1]\,r\mathrm{d}r=0. \tag{37}$$

This technique is known as the isotherm method.[19]

The Galerkin method is applied to the stress-divergence form of the momentum, (4), and continuity, (6), equations to yield residual equations for the velocity and pressure fields in the melt:

$$\int_{D_m}[\nabla\boldsymbol{\Phi}^i:\boldsymbol{\sigma}-\boldsymbol{\Phi}^i\mathbf{v}:\nabla\mathbf{v}-(\boldsymbol{\Phi}^i\cdot\mathbf{e}_z)\,GrPr^2(T-1)]\,\mathrm{d}V+\oint_{\partial D_m}\boldsymbol{\Phi}^i\mathbf{n}:\boldsymbol{\sigma}\,\mathrm{d}S=0, \tag{38}$$

where $i=1, \ldots, N_m$ represents the residual equation for each node in the melt and $\{\boldsymbol{\Phi}^i\}$ represents the velocity basis functions of (31) multiplied by the three unit vectors $(\mathbf{e}_r, \mathbf{e}_z, \mathbf{e}_\theta)$ for each component of the velocity field. In this notation (38) has a total of $N_v=3N_m$ residual equations which describe the velocity in the melt. The continuity equation is discretized using Galerkin's method to yield

$$\int_{D_m}\Psi^j\nabla\cdot\mathbf{v}\,\mathrm{d}V=0, \tag{39}$$

where $j=1, \ldots, N_p$.

At the centreline of the melt equations (18) are applied as natural boundary conditions for v_z and T, and equations (19) are enforced as essential boundary conditions on v_r and v_θ along the melt/crystal interface and the bottom and sides of the crucible. No-slip conditions (20)–(23) are applied as essential boundary conditions. Since the melt meniscus is a free surface, one boundary condition must be *distinguished* for determining its location while the remaining three are used as boundary conditions for the three components of the momentum equation. The azimuthal component of surface stress, (25), is applied as a natural condition for v_θ. The remaining tangential stress balance (26) and the kinematic condition (24) are applied as boundary conditions for v_r and v_z, respectively. The tangential stress balance (26) is included as a weak boundary condition. No normal flow through the melt/crystal and meniscus surfaces is enforced by the residual equations

$$\int_{\partial D_0} \Phi^i \mathbf{v}\cdot\mathbf{n}_0 \, \mathrm{d}S = 0, \tag{40}$$

$$\int_{\partial D_1} \Phi^i \mathbf{v}\cdot\mathbf{n}_1 \, \mathrm{d}S = 0, \tag{41}$$

which replace the z-component of the momentum equation along the interface.

It is crucial for self-consistent conservation of mass that the integral formulation of the no-penetration condition is used on both curved boundaries. Calculations based on the integral formulation (41) along the meniscus, but setting $v_r = v_z = 0$ as essential boundary conditions on the melt/crystal interface in place of (40) (including the node at the tri-junction), resulted in poor conservation of mass in the element under the meniscus next to the tri-junction. The failure to obey mass conservation is closely allied with the loss of the hydrostatic pressure mode that must exist for incompressible flow.[34] In this case the error in mass conservation from the small element adjoining the tri-junction was severe enough to drive weak, secondary vortices in this region. These vortices are not seen when the weak form (40) is used.

As in the conduction-dominated TCM, the normal stress condition at the meniscus is used as the distinguished condition for this interface. The weak form of this equation is

$$-\int_R^1 \left(\frac{(\Gamma^i)' H_1'}{\sqrt{(1+(H_1')^2}} + \Gamma^i [Bo(H_1+\lambda) - We\,\mathbf{n}_1\mathbf{n}_1 : \boldsymbol{\sigma}] \right) r \mathrm{d}r = 0, \tag{42}$$

with the boundary conditions (17) and (18) applied. For $We = 0$ this result is identical to the discretized form of the Young–Laplace equation of capillary statics used by Derby *et al.*[12]

The volume constraint (14) and the wetting angle condition (15) complete the set of residual equations for the reference pressure difference λ and the crystal radius R respectively. The volume constraint is formulated by writing the interface shape functions $H_0(r)$ and $H_1(r)$ in terms of their one-dimensional Lagrangian basis functions and using three-point Gaussian quadrature to evaluate the integrals along the element boundaries on ∂D_0 and ∂D_1.

3.2. *Newton/Raphson method*

The set of non-linear residual equations which describes this problem is formed by the combination of equations (14), (15) and (36)–(42). The non-linearities are provided by the temperature-dependent thermal conductivity, the radiation boundary flux conditions for the energy equations, the convective transport terms in the momentum and energy equations, the mean curvature in the normal force balance across the meniscus and, most pervasively, the dependence of all the residuals on the interface shapes through the implicit dependence of the finite element basis functions and the Galerkin integrals on the domain shape. The performance of any numerical algorithm for such a complex free boundary problem depends strongly on the method employed to solve this non-linear equation set.

We have extended the Newton/Raphson method applied for the conduction-dominated TCM to include the velocity and pressure unknowns in the melt. We summarize the technique here; more detail is available in Reference 35.

The set of residual equations (36)–(42) is represented by the vector equation

$$\mathbf{R}(\mathbf{x};\mathbf{p})=\mathbf{0}. \tag{43}$$

The vector of unknowns is $\mathbf{x}=(\mathbf{T}, \mathbf{v}_r, \mathbf{v}_z, \mathbf{v}_\theta, \mathbf{P}, R, \mathbf{H}_0, \mathbf{H}_1, \lambda)$, where the unknown field variables are represented by vectors of their nodal values. The vector $\mathbf{p}$ represents the parameters in the equation set. As discussed in Section 2.3, in the calculations performed here the heater temperature T_H is included as an unknown in the simulation by adding equation (27). Then T_H is removed from $\mathbf{p}$ and added to $\mathbf{x}$.

The Newton/Raphson iteration scheme is used to solve simultaneously for all unknowns. Given an initial guess for the solution $\mathbf{x}^{(0)}$, successive iterations are computed as

$$\mathbf{x}^{(k+1)}=\mathbf{x}^{(k)}+\boldsymbol{\delta}^{(k)}, \tag{44}$$

where k denotes the iteration number and the correction vector $\boldsymbol{\delta}^{(k)}$ is calculated by solving the linear equation set

$$\mathbf{J}(\mathbf{x}^{(k)})\boldsymbol{\delta}^{(k)}=-\mathbf{R}(\mathbf{x}^{(k)};\mathbf{p}) \tag{45}$$

where $J_{ij}=\partial R_i/\partial x_j$, is the Jacobian matrix representing the sensitivity of the residual equation set with respect to the unknowns. All contributions to the Jacobian matrix are computed in closed form. The procedure described in Reference 35 is used to account for the dependence of the basis functions on the locations of the nodes $\{r_i, z_i\}$ and hence on the shape of the interfaces.

The linear equation set (45) is solved by Gaussian elimination using a modified frontal solver based on the one originally put forth by Hood.[36] Buffering and asynchronous I/O are implemented to maximize computational efficiency on Cray X-MP computers at Lawrence Livermore Laboratory and Pittsburgh Supercomputing Center.

Including the unknowns due to the interfaces in the simultaneous solution algorithm is particularly efficient and robust. Typically, between three and six Newton iterations are required to converge to a solution, depending on the values of the parameters and the initial guess used in (44)–(45). In addition, Newton's method lends itself to computer-implemented perturbation methods for determining the temporal stability of the solution, to continuation methods for generating accurate initial guesses and for traversing folds in the parameter space[37] and to the formulation of fully implicit transient integration methods.[35]

4. RESULTS FOR SILICON GROWTH

The thermophysical properties and system parameters used in the simulation of silicon crystal growth are given in Tables II and III. For the calculations presented here, the radius of the crucible is $R_{\mathrm{cruc}}=7{\cdot}3025$ cm and the crystal radius set point in (27) is $R_{\mathrm{set}}=0{\cdot}5\,R_{\mathrm{cruc}}$. All of the parameter values in the simulations presented here were set at those listed in these tables, except that the possiblity of surface-tension-driven flows was ignored ($\mathrm{d}\gamma/\mathrm{d}T=0$) and the coefficient of thermal expansion was used as a parameter to vary the intensity of the buoyancy-driven flows from $\beta_{\mathrm{m}}=0\,K^{-1}$, corresponding to the conduction-dominated model, to the value $\beta_{\mathrm{m}}=1{\cdot}4\times10^{-4}\,K^{-1}$, appropriate for Si. The crystal radius is held fixed for all the calculations reported here by using the extra equation (27) to determine the appropriate heater temperature T_{H}. The more effective heat

Table II. Thermophysical data used for HTCM simulations of silicon and GGG growth systems

Quantity	Symbol (units)	Silicon				GGG		
		D_m	D_s	D_c	D_l	D_m	D_s	D_c
Heat capacity	$C_p(\mathrm{J\,g^{-1}\,K^{-1}})$	1·0	2·3	1·6	2·2	0·586	0·586	1·0
Thermal conductivity	$k\ (\mathrm{W\,cm^{-1}\,K^{-1}})$	0·64	0·22	0·60	0·06	0·05	0·20	1·5
Density	$\rho(\mathrm{g\,cm^{-3}})$	2·42	2·3	1·6	2·2	5·7	7·2	22·4
Emissivity	$\varepsilon(1)$	0·3	0·7	0·8	0·35	0·3	0·3	0·5

Quantity	Symbol (units)	Silicon	GGG
Thermal diffusivity in melt	$\alpha_m\ (\mathrm{cm^2\,s^{-1}})$	0·26	0·015
Thermal diffusivity in crystal	$\alpha_s\ (\mathrm{cm^2\,s^{-1}})$	0·096	0·047
Viscosity	μ_m (cP)	0·7	40.
Kinematic viscosity	$\nu_m\ (\mathrm{cm^2\,s^{-1}})$	$2{\cdot}9\times10^{-3}$	$7{\cdot}0\times10^{-2}$
Coefficient of thermal expansion	$\beta_m\ (\mathrm{K^{-1}})$	$0\text{–}1\times10^{-4}$	$0\text{–}2{\cdot}7\times10^{-5}$
Heat of fusion	$\Delta H_f\ (\mathrm{J\,g^{-1}})$	1800.	455.4
Melting point temperature	T_{mp} (K)	1683	2023
Equilibrium growth angle	ϕ_0 (deg)	11	17
Surface tension	$\gamma\ (\mathrm{dyne\,cm^{-1}})$	742·6	700·0
Thermocapillary coefficient	$\mathrm{d}\gamma/\mathrm{d}T\ (\mathrm{dyne\,cm^{-1}\,K^{-1}})$	0	0

Table III. Operating parameters for HTCM simulations for silicon and GGG

Quantity	Symbol (units)	Silicon	GGG
Crucible radius	L (cm)	7·3025	9·8425
Melt volume	$V_m\ (\mathrm{cm^3})$	973	953
Pull rate	$V_g\ (\mathrm{cm\,h^{-1}})$	5·0	0·1
Heater temperature	T_H (K)*	1902†	2412‡
Crystal rotation rate	ω_s (rpm)	0	0
Crucible rotation rate	ω_c (rpm)	0	0
Ambient temperature	T_a (K)	1430	1800
Set point radius	R_{set} (R_{cruc})*	0·5	0·5
External convective heat transfer coefficient	$h\ (\mathrm{W\,cm^{-2}\,K^{-1}})$	0·001	0·001

* Note that heater temperature and crystal radius are coupled through the control equation.
† Computed *ex post facto* for the case $\beta_m = 2\times10^{-6}\ \mathrm{K^{-1}}$ ($Gr^* = 7\times10^6$, $Re^* = 2100$) for mesh M5.
‡ Computed *ex post facto* for the case $\beta_m = 2{\cdot}7\times10^{-5}\ \mathrm{K^{-1}}$ ($Gr^* = 1{\cdot}8\times10^6$, $Re^* = 840$) for mesh N3.

transport by convection will cause T_H to decrease with increasing β_m. Then the effective Grashof number Gr^* will vary because of both β_m *and* ΔT_m.

Computations were performed for the three different meshes shown in Figure 4. The coarsest mesh, M3, is identical to the finest mesh used for the conduction-dominated TCM by Derby.[15] This mesh consisted of 16 radial elements and eight axial elements in the melt plus a thin special graded region containing four elements in the radial direction just outside the growth tri-junction. This region is included so that the highly curved melt/ambient surface is accurately represented.

The mesh M3 was more than adequate to represent the temperature field for the TCM but was generally insufficient to resolve the velocity field for intense flows. Consequently two finer meshes were constructed. The intermediate mesh, M4, was designed from M3 by adding extra elements in the graded regions on the boundaries. This was done to help capture the boundary layer structure in the velocity field for intense convection. The finest mesh, M5, was constructed from M4 by increasing the number of elements in the bulk regions of the melt to $32r \times 16z$ but retaining the same discretization near the boundaries. The detailed picture of the melt region of mesh M5 given in Figure 6 depicts the special layers and shows the deformation of the elements required to map the interface shapes.

The calculations presented here focus only on buoyancy-driven flows as a demonstration of the accuracy of the calculations. Results for combinations of the possible driving forces will be presented elsewhere.

4.1. Increasing buoyancy-driven convection

The evolution of the flow pattern in the melt for increasing Grashof number is demonstrated in Figures 7 and 8 by results with the finest mesh M5 for increasing β_m. Streamline and temperature

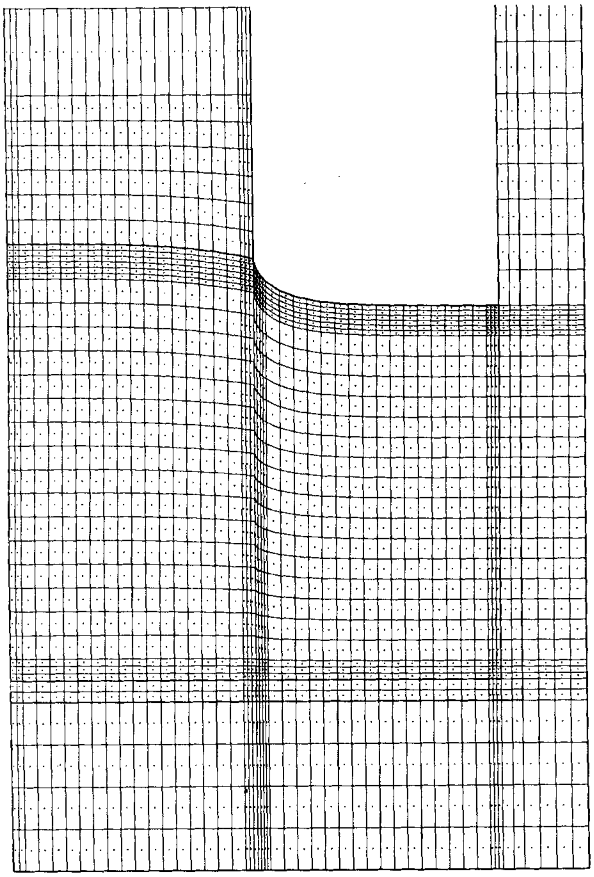

Figure 6. Detailed view of the finite element mesh M5 in the melt region

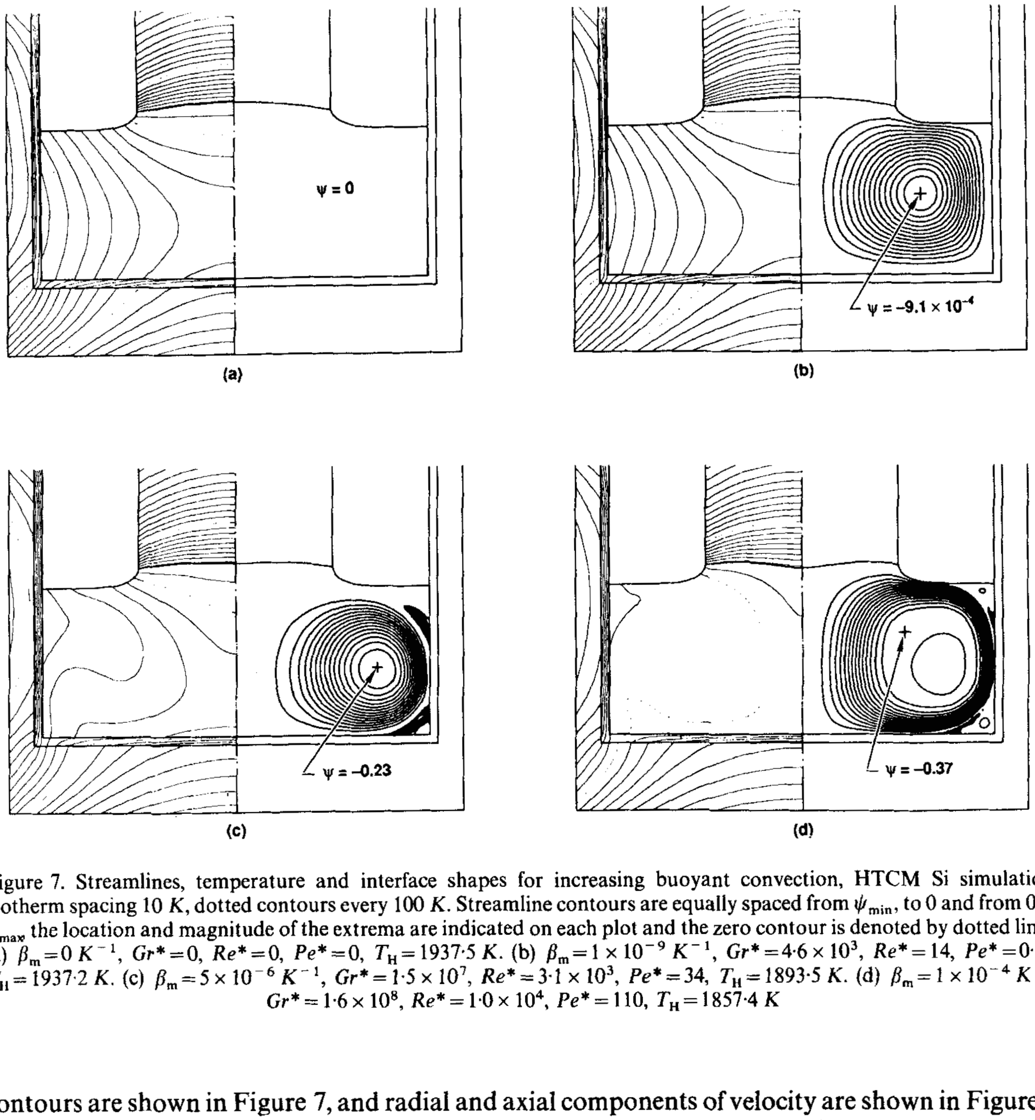

Figure 7. Streamlines, temperature and interface shapes for increasing buoyant convection, HTCM Si simulation. Isotherm spacing 10 K, dotted contours every 100 K. Streamline contours are equally spaced from $\psi_{\min}$, to 0 and from 0 to $\psi_{\max}$, the location and magnitude of the extrema are indicated on each plot and the zero contour is denoted by dotted lines. (a) $\beta_m = 0\ K^{-1}$, $Gr^* = 0$, $Re^* = 0$, $Pe^* = 0$, $T_H = 1937{\cdot}5\ K$. (b) $\beta_m = 1 \times 10^{-9}\ K^{-1}$, $Gr^* = 4{\cdot}6 \times 10^3$, $Re^* = 14$, $Pe^* = 0{\cdot}15$, $T_H = 1937{\cdot}2\ K$. (c) $\beta_m = 5 \times 10^{-6}\ K^{-1}$, $Gr^* = 1{\cdot}5 \times 10^7$, $Re^* = 3{\cdot}1 \times 10^3$, $Pe^* = 34$, $T_H = 1893{\cdot}5\ K$. (d) $\beta_m = 1 \times 10^{-4}\ K^{-1}$, $Gr^* = 1{\cdot}6 \times 10^8$, $Re^* = 1{\cdot}0 \times 10^4$, $Pe^* = 110$, $T_H = 1857{\cdot}4\ K$

contours are shown in Figure 7, and radial and axial components of velocity are shown in Figure 8 along with the pressure field. Since there is no driving force for rotational flow, i.e. $Re_s = Re_c = 0$, the azimuthal velocity is zero in all cases. The temperature field for pure conduction ($\beta_m = 0\ K^{-1}$) is shown for reference in Figure 7(a). Heat enters non-uniformly along the wall of the crucible and conducts through the melt into the crystal and the crucible bottom. Heat is lost from the crystal, crucible and melt surfaces by radiation and conduction according to (11). The radial temperature gradients in the melt lead to buoyancy-driven flows for any non-zero value of β_m. Several flow regimes are apparent as β_m is increased. These regimes represent changes in the dominant forces in the momentum balance, the formation of boundary layers and the growing importance of convective heat transport.

For very low values of the thermal expansion coefficient, $\beta_m < 10^{-9}\ K^{-1}$, the structure of the flow is controlled by a balance of viscous and buoyant forces. Under these conditions the Reynolds number $Re^* \equiv V^* R_c / \nu_m$ based on the characteristic velocity of the melt, V^*, is small; $Re^* < 10$ approximately. Then the Peclet number for convective heat transport, $Pe^* \equiv Re^* Pr$, is

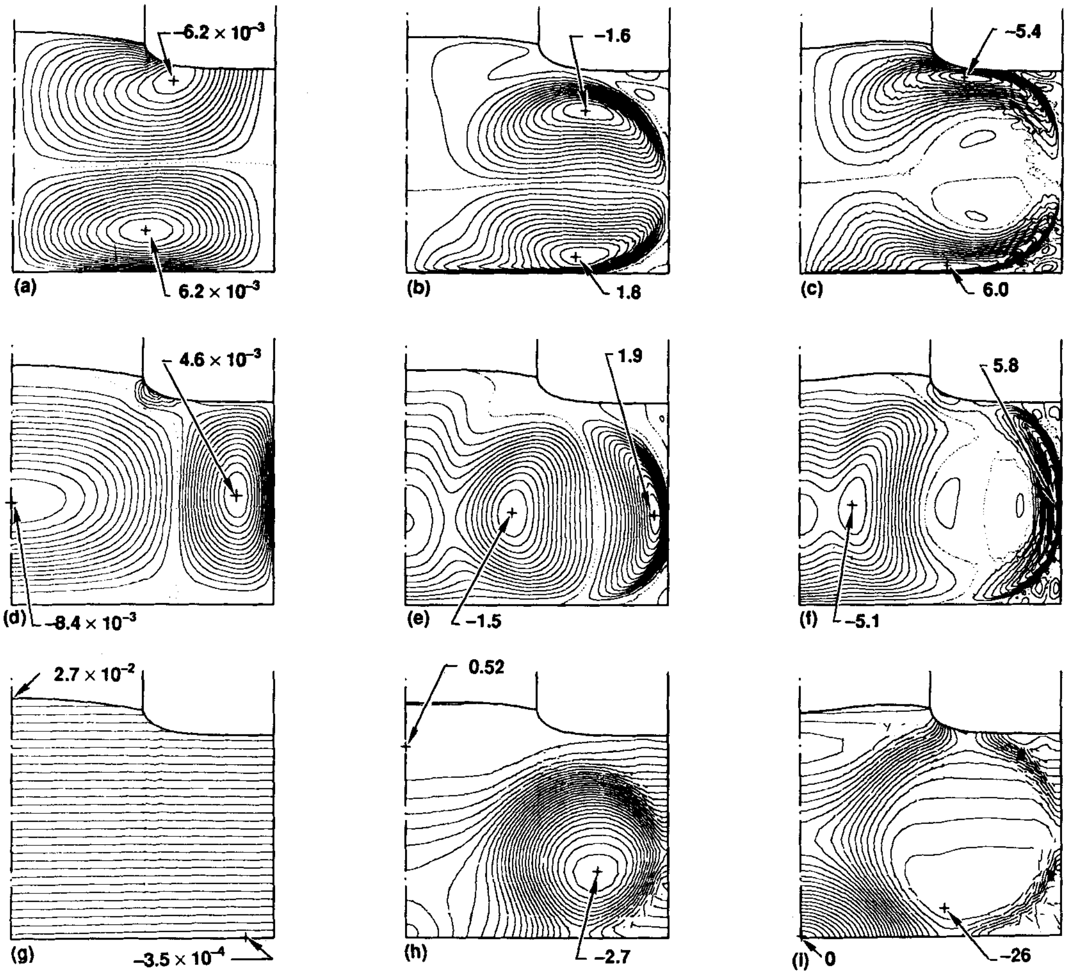

Figure 8. Contours of v_r, v_z, and P_* for increasing β_m, HTCM Si simulation. Velocity contours are equally spaced from the minimum to zero and from zero to the maximum, with the location and magnitude of the extrema indicated on each plot and the zero contour denoted by dotted lines. Pressure contours are equally space between P_{min} and P_{max}. Radial velocity contours for (a) $\beta_m = 1 \times 10^{-9}\ K^{-1}$, (b) $\beta_m = 5 \times 10^{-6}\ K^{-1}$, (c) $\beta_m = 1 \times 10^{-4}\ K^{-1}$. Axial velocity contours for (d) $\beta_m = 1 \times 10^{-9}\ K^{-1}$, (e) $\beta_m = 5 \times 10^{-6}\ K^{-1}$, (f) $\beta_m = 1 \times 10^{-4}\ K^{-1}$. Pressure contours for (g) $\beta_m = 1 \times 10^{-9}\ K^{-1}$, (h) $\beta_m = 5 \times 10^{-6}\ K^{-1}$, (i) $\beta_m = 1 \times 10^{-4}\ K^{-1}$

also small (for silicon $Pr = 0{\cdot}01$) so that the temperature field stays very near the conduction-dominated limit.

Increasing β_m, and hence Gr^*, rapidly forces inertia to become important in the flow and leads to the formation of an inviscid core flow which is connected to the solid surfaces by viscous boundary layers; the flow in Figures 7(b) and 8(a, d, g) for $\beta_m = 1 \times 10^{-9}\ K^{-1}(Gr^* = 5 \times 10^3)$ is an example of this type of flow. The formation of the boundary layer on the vertical sidewall is very evident in the axial velocity component v_z; the boundary layer along the bottom of the crucible is clear in the contours of v_r. The inviscid motion in the core of the vortex produces pressure contours which follow Bernoulli's equation, i.e. $P \propto |\mathbf{v}|^2$; see Figure 8(h).

The boundary layers separate from the crucible bottom and sidewall as β_m is increased. The resulting steady state flows with small separated eddies, as shown in Figure 7(c) for

$\beta_m = 5 \times 10^{-6}\ K^{-1}$ ($Gr^* = 1{\cdot}5 \times 10^7$), are probably unstable to oscillatory disturbances which lead to time-periodic solutions like the ones computed by Crochet *et al.*[24] and Bottaro and Zebib.[38] Thermal boundary layers have not yet formed in the melt; $Pe^* = 34$ for $\beta_m = 5 \times 10^{-6}\ K^{-1}$.

Increasing β_m towards the value $1{\cdot}4 \times 10^{-4}$ that is appropriate for silicon[39] leads to thermal boundary layers along the crucible bottom and sidewall and to a nearly isothermal core region in the melt. Then the melt motion is fastest in a boundary layer adjacent to the sidewall and this layer separates from the sidewall and circulates around the melt cavity. A sample flow pattern is shown in Figure 7(d) for calculations with $\beta_m = 1 \times 10^{-4}\ K^{-1}$ ($Gr^* = 1{\cdot}6 \times 10^8$). Under these conditions the melt in the centre of the crucible moves very slowly clockwise and the pressure field is approximately hydrostatic there. The weak counter-rotating core flow is driven by the inverted radial temperature gradient in this region and opposed by shear forces acting from the boundary layers. A similar concentric counter-rotating core flow is evident in the bulk flow simulations of Langlois and Lee.[39]

The evolution of the heater temperature T_H and the effective Reynolds number Re^* with increasing buoyant convection as measured by Gr^* are plotted in Figure 9. For values of

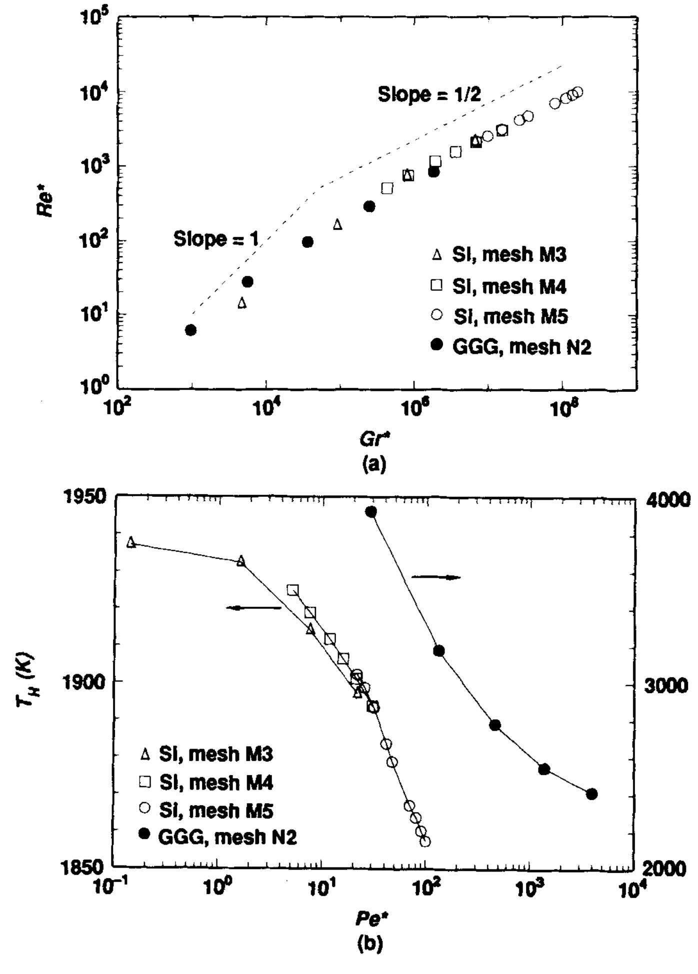

Figure 9. Reynolds number Re^* as a function of Gr^*, and the heater temperature $T_H(K)$, required to maintain the constant crystal radius, as a function of Pe^*

$Gr^* > 1 \times 10^6$, Re^* grows as $Gr^{*\,1/2}$ and T_H decreases as $Gr^{*\,1/2}$, as predicted by the analysis of a buoyant boundary layer on a vertical surface of fixed temperature.[40]

The complex flow structure, including extremely fine boundary layers, makes even the computation in fixed domains of CZ bulk flow difficult. The calculations shown in Figures 7 and 8 demonstrate these features. Moreover, the wiggles in the velocity contours near the bottom and sidewall boundary layers for $\beta_m = 1 \times 10^{-4}\ K^{-1}$ (Figure 8(c, f)) show that even the finest mesh is beginning to have difficult approximating the flow.[41] This difficulty is not surprising considering that $Re^* = O(10^4)$.

The robustness of the simultaneous Newton iteration for the field variables and interface shapes is evident in Figure 10 by the convergence with the number of Newton iterations for calculations with increasing β_m. Initial guesses for each calculation were provided either by using the converged solution at the closest lower value of β_m, or by extrapolating with a polynomial fit of two or more previous converged solutions. In each calculation the iterations converged quadratically after one or two initial iterations.

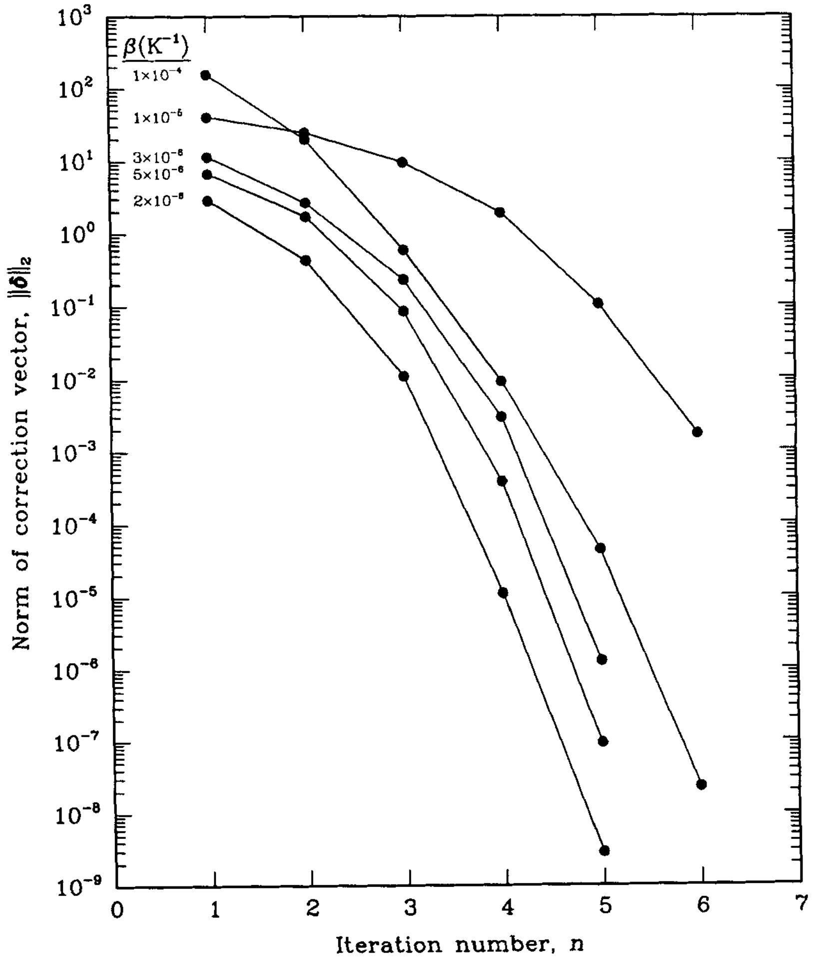

Figure 10. Convergence of Newton iteration scheme for different values of β_m

4.2. *Flow near the tri-junction*

The predictions of the asymptotic analysis for the structure of the velocity field near the tri-junction are tested by plotting the form of the velocity components $v_r(R, z)$ and $v_z(R, z)$ as the tri-junction is approached upward along a ray at a constant value of the radial co-ordinate, $r=R$. Along this vertical line, the radial and vertical velocity components (v_r, v_z) measured in the global cylindrical co-ordinate system are identical with the azimuthal and radial velocity components (v_ϑ, v_ρ) measured in the local polar co-ordinate system originating at the tri-junction; see Figure 2. The results for calculations with four meshes with equally spaced elements in the melt and with $\beta_m = 1 \times 10^{-8}\ K^{-1}$ are shown in Figure 11(a) for $\phi_0 = 45°$ with ns/ns boundary conditions and in Figure 11(b) for $\phi_0 = 90°$, a flat meniscus, for ns/sf boundary conditions. Recalling that the exponent for the local tri-junction velocity components is $\lambda - 1$, we extract the finite element prediction for λ_r from a logarithmic plot of $|v_\vartheta|$ as a function of ρ, the distance to the tri-junction. The leading-order power law behaviour predicted by the form (28) is evident in both results. The exponents predicted by the calculations also agree with the asymptotic values. For $\phi_0 = 45°$, $\lambda_{calc} = 2{\cdot}74$ and $\lambda_r = 2{\cdot}63$ and for $\phi_0 = 90°$, $\lambda_{calc} = 1{\cdot}50$ and $\lambda_r = 1{\cdot}5$.

4.3. *Assessment of accuracy*

We have assessed the accuracy of the finite element algorithm by comparing claculations at $\beta_m = 5 \times 10^{-6}\ K^{-1} (Gr^* = 1{\cdot}5 \times 10^7)$ for the three meshes shown in Figure 4. Contours of the two velocity components, the streamfunction, temperature and pressure are shown separately. The qualitative features of the temperature field and the streamfunction shown in Figures 12 and 13 are similar for each mesh and provide a flattering but incomplete indication of the accuracy of the calculation. The size, intensity and location of the separated eddies vary significantly with mesh refinement, indicating that meshes M3 and M4 are too coarse to capture these aspects of the flow.

The inadequate resolution of meshes M3 and M4 is evident in the contours of velocity shown in Figures 14 and 15. Only the finest mesh M5 gives velocity fields free of oscillations. Because the flow field is relatively inviscid away from the solid boundaries, the inaccuracies in the velocity field are mimicked by the pressure (Figure 16) through Bernoulli's equation.

A quantitative comparison of results for the three meshes is given in Table IV. Each of the measures of the solution converge with increasing mesh refinement, i.e. the difference between the results for meshes M3 and M4 is greater than the difference between the calculations for meshes M4 and M5. The convergence of these results is not a trivial test for calculations. Because the Grashof number is high enough for the formation of viscous boundary layers, the calculation of the flow field is extremely difficult. Much more impressive convergence results can be tabulated for the viscous-dominated flows for $Gr^* < 10^5$, but the results are less meaningful for the prediction of real flow phenomena in CZ growth.

We have found that examining contours of the divergence of the velocity field $(\nabla \cdot \mathbf{v})$ is an effective means for detecting the local breakdown of the accuracy of the calculations as well as for diagnosing improper formulation of the discretized equations for mass conservation on the boundary alluded to in Section 3.1. This is demonstrated in Figure 17 by plots of $(\nabla \cdot \mathbf{v})$ for calculations with meshes M3, M4 and M5 and the value of β_m used in Figure 4. Because $(\nabla \cdot \mathbf{v})$ is calculated by simply differentiating the Lagrangian biquadratic basis functions for $\mathbf{v}$, the contours are discontinuous across element boundaries.

For the coarse mesh M3 in Figure 17(a) the pointwise error in $(\nabla \cdot \mathbf{v})$ is distributed throughout the flow and reaches extreme values of 17. Because the zero contour is present in each element and the positive and negative pointwise deviations are such that the imposed Galerkin integral

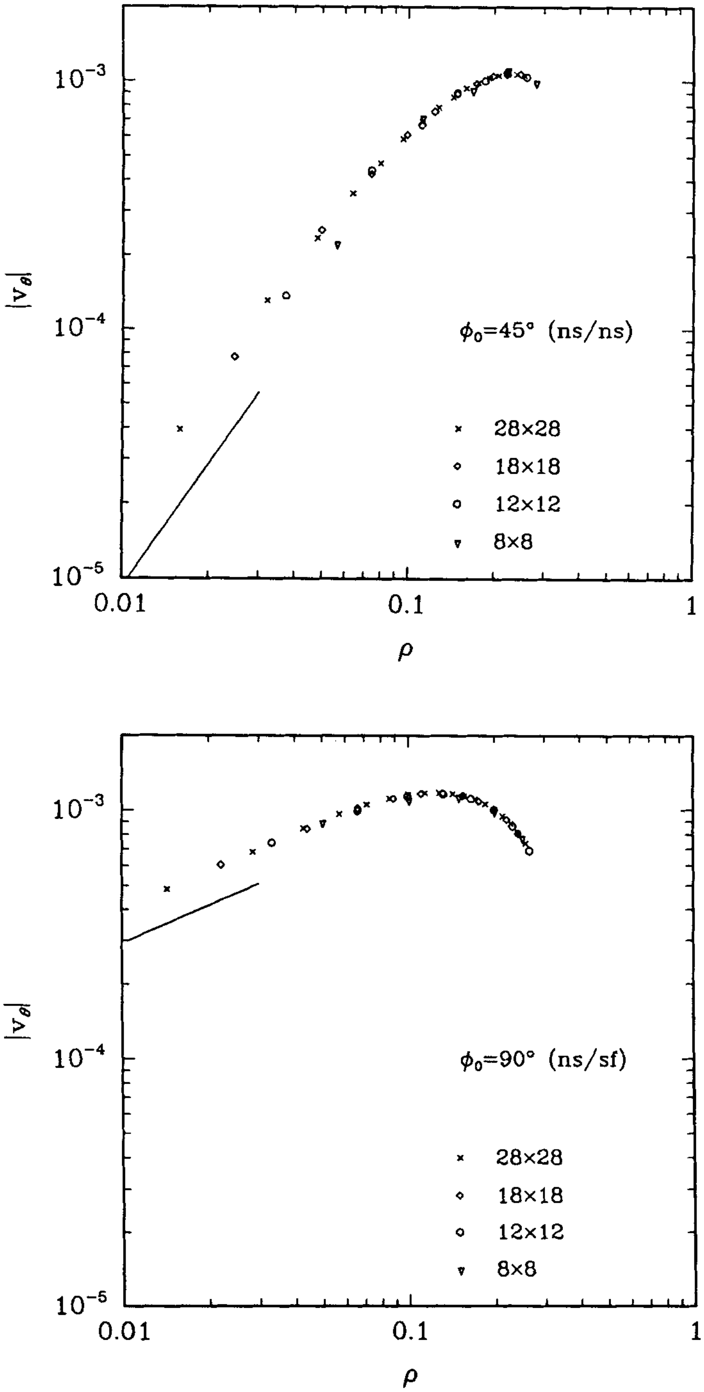

Figure 11. Velocity and pressure field in the vicinity of the tri-junction, plotted along the vertical line at $r=R$. Following this ray to the tri-junction, $\rho \equiv H_1(R,z)-z$, $v_\rho \equiv v_r$, $v_\vartheta \equiv v_z$

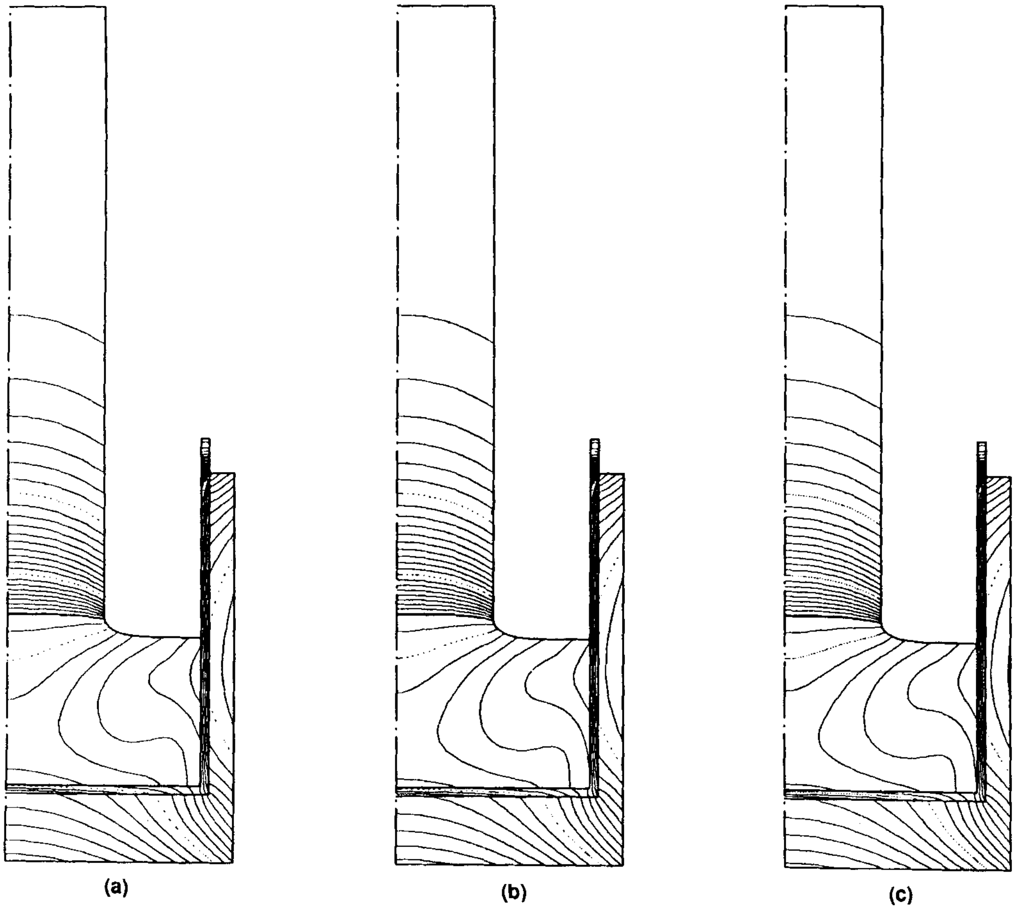

Figure 12. Temperature contours for HTCM Si simulation for $\beta_m = 2 \times 10^{-6}\ K^{-1}$, $Gr^* = 7 \times 10^6$, $Re^* = 2100$. Isotherm spacing 10 K, dotted contours every 100 K. Meshes: (a) M3, (b) M4, (c) M5

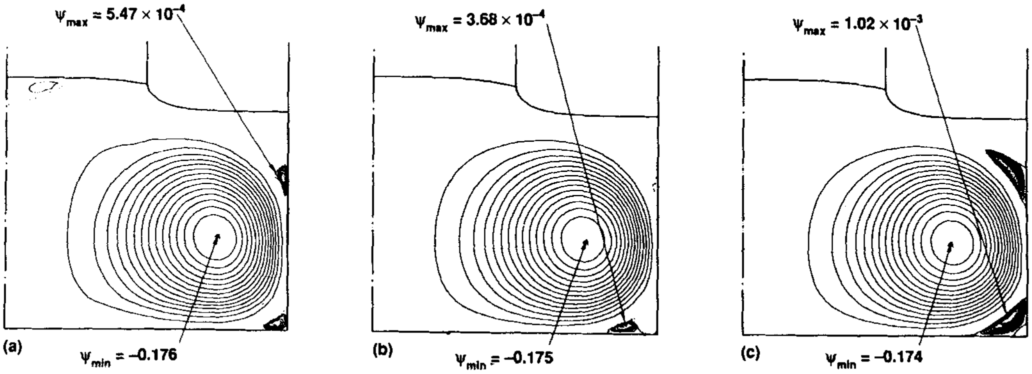

Figure 13. Stream function contours for HTCM Si simulation for $\beta_m = 2 \times 10^{-6}\ K^{-1}$, $Gr^* = 7 \times 10^6$, $Re^* = 2100$. Contour values evenly spaced between ψ_{min} (M5) and zero and between zero and ψ_{max} (M5); zero contour denoted by a dotted line. Extrema are indicated for each plot. Meshes: (a) M3, (b) M4, (c) M5

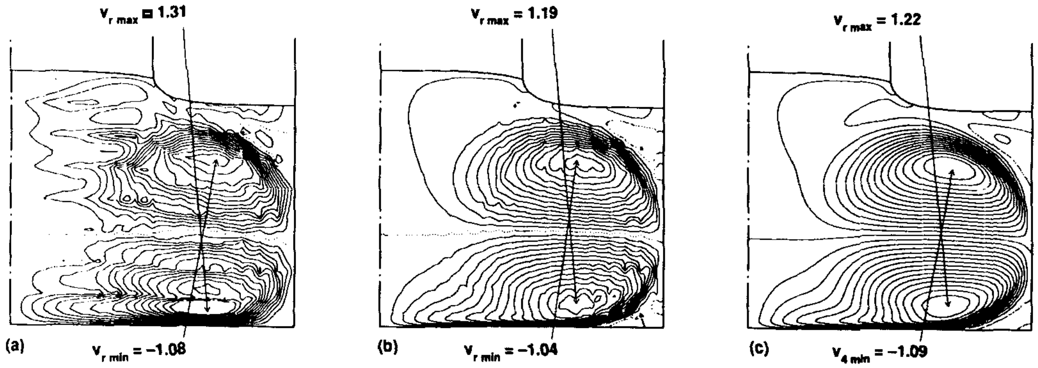

Figure 14. Radial velocity contours for HTCM Si simulation for $\beta_m = 2 \times 10^{-6}\ K^{-1}$, $Gr^* = 7 \times 10^6$, $Re^* = 2100$. Contour values evenly spaced between $v_{r_{\min}}$ (M5) and zero and between zero and $v_{r_{\max}}$ (M5); zero contour denoted by a dotted line. Extrema are indicated for each plot. Meshes: (a) M3, (b) M4, (c) M5

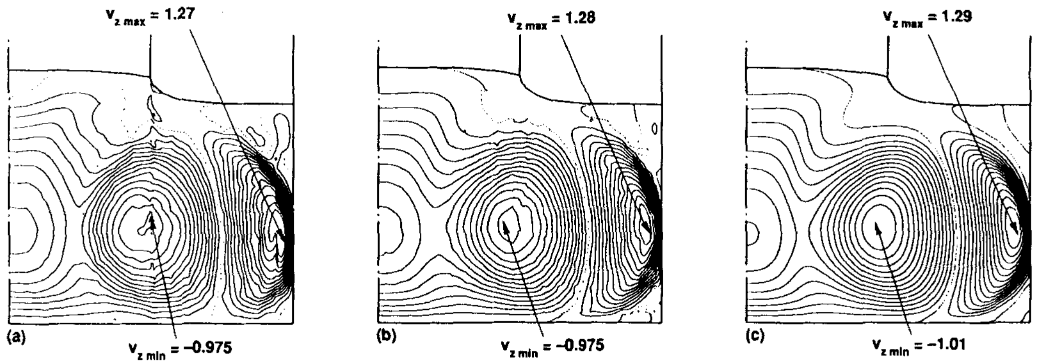

Figure 15. Axial velocity contours for HTCM Si simulation for $\beta_m = 2 \times 10^{-6}\ K^{-1}$, $Gr^* = 7 \times 10^6$, $Re^* = 2100$. Contour values evenly spaced between $v_{z_{\min}}$(M5) and zero and between zero and $v_{z_{\max}}$(M5); zero contour denoted by a dotted line. Extrema are indicated for each plot. Meshes: (a) M3, (b) M4, (c) M5

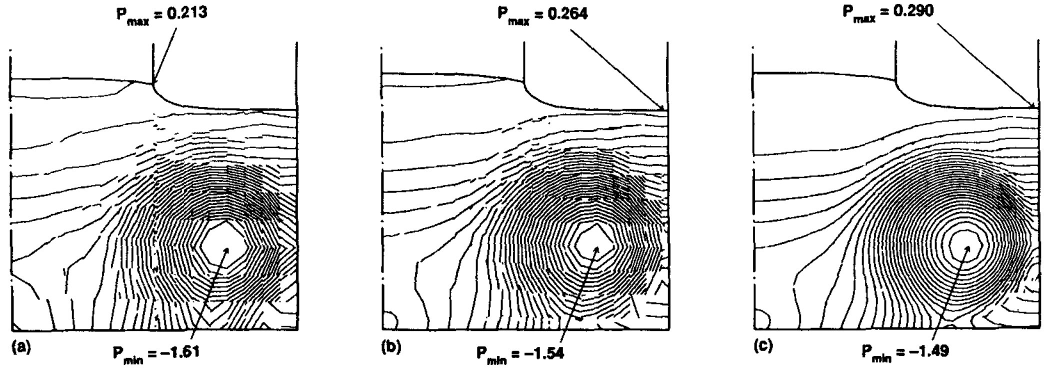

Figure 16. Pressure contours for HTCM Si simulation for $\beta_m = 2 \times 10^{-6}\ K^{-1}$, $Gr^* = 7 \times 10^6$, $Re^* = 2100$. Contour values evenly spaced between $P_{\min}$(M5) and $P_{\max}$(M5). Extrema are indicated for each plot. Meshes: (a) M3, (b) M4, (c) M5

Table IV. Measures of overall solution obtained for three different meshes for Si growth

Description	Variable	M3	M4	M5
No. of radial elements in melt	NE_{mr}	20	28	44
No. of axial elements in melt	NE_{mz}	8	17	25
No. of velocity unknowns in melt	N_{v}	2091	5985	13617
No. of pressure unknowns in melt	N_{p}	480	1428	3300
Total no. of unknowns	N_{tot}	6647	13999	28287
CPU sec/Newton iteration		20	50	170
Streamfunction minimum	ψ_{min}	−0·17600	−0·17530	−0·17351
Streamfunction maximum	ψ_{max}	$5{\cdot}468 \times 10^{-4}$	$3{\cdot}684 \times 10^{-4}$	$1{\cdot}025 \times 10^{-3}$
Temperature difference across melt domain	ΔT_{melt}	0·042788	0·044147	0·044633
Heater temperature	T_{H}	1·127213	1·129649	1·130362
Melt/crystal interface deflection	$\lvert\Delta H_0\rvert$	−0·02075	−0·03009	−0·03176
Grashof no.	Gr^*	$6{\cdot}574 \times 10^{6}$	$6{\cdot}782 \times 10^{6}$	$6{\cdot}857 \times 10^{6}$
Reynolds no.	Re^*	2170	2110	2150
Range of pressure	ΔP	1·8106	1·7421	1·7547

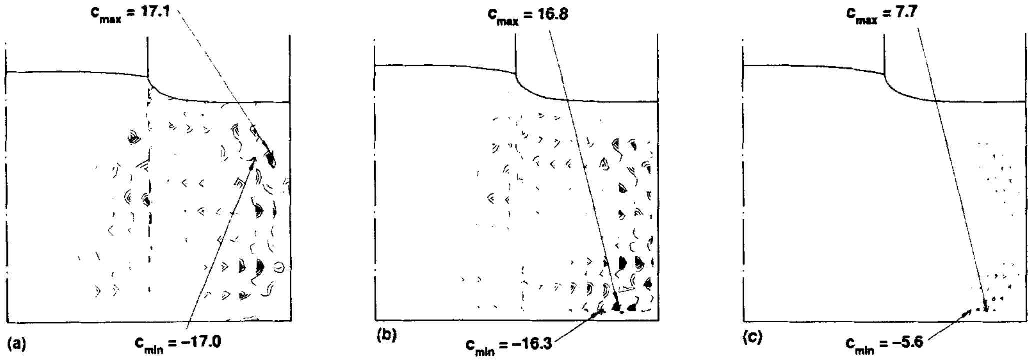

Figure 17. Contours of $(\nabla \cdot \mathbf{v})$. Contours plotted for $(\nabla \cdot \mathbf{v}) = 0{\cdot}1,\ 1{\cdot}0,\ 10$ for meshes: (a) M3, (b) M4, (c) M5

residual equation is satisfied, it is both sufficient and more illuminating to plot only the contours of one sign. There is some focusing of the error in the highly deformed isoparametric elements under the tri-junction. The error is greater in the boundary layers, and especially in regions of separated flow, as seen in Figure 17(c) for mesh M5. This indicates a deterioration in the quality of the velocity field which is also seen in the contour maps for v_r and v_z.

5. RESULTS FOR GGG GROWTH

The system parameters and thermophysical properties used in the calculations for GGG are given in Tables II and III. The dimensions of the system match the experimental CZ apparatus of the LLNL Laser Program with a crucible radius of 4 inches and a crucible height of 8 inches. Simulations for increasing β_{m} were carried out to examine the effect of increasing the intensity of buoyancy-driven convection in the melt. As discussed previously, this approach allows for the independent variation of the Grashof number in the model. The calculations presented in the following sections do not include rotation of the crystal or crucible, nor is thermocapillarity considered. Results for combinations of driving forces will be considered in another paper. As in the results for Si, the crystal radius is set to $R_{cruc}/2$ and the heater temperature T_H, consistent with the fixed radius, is calculated as part of the solution.

The high Prandtl number ($Pr \approx 4{\cdot}7$) of molten GGG and the range of Grashof numbers considered here ($Gr^* \approx 10^3 - 10^6$) virtually assure the development of boundary layers in the temperature and velocity field as the intensity of flow increases. Accordingly, finite element meshes were carefully designed to adequately capture this behaviour, with fine elements near the boundaries of the flow domain. As for the meshes used in the silicon calculations, additional elements were also included to resolve the shape of the highly curved meniscus and the details of the flow field near the sharp corner formed by the melt/crystal interface and the melt meniscus. The three meshes N1–N3 used in the calculations are shown in Figure 5. Mesh N2, with a total of 28 419 unknowns, was used for all of the results presented in Section 5.1. The accuracy of these meshes is addressed in Section 5.2.

5.1. *Increasing buoyancy-driven convection*

The temperature and flow fields for calculations of increasing β_m and Gr^* are shown in Figures 18 and 19. The temperature field and interface shapes for a hypothetical system with no convection ($\beta_m = 0\ K^{-1}$, $Gr^* = 0$) are shown for reference in Figure 18(a). Although this temperature field is similar to the result for silicon shown in Figure 7(a), there are several important quantitative differences. First, the melt/crystal interface is appreciably more concave. This is caused by the larger radial temperature gradients in the crystal due to the enhanced radiative heat loss at the higher temperature. Secondly, the axial temperature gradient in the crystal is lower than that in the melt because the conductivity of the crystal is three times higher. This situation is opposite to that in silicon growth.

The larger Prandtl number of GGG, $Pr \approx 4{\cdot}7$, causes the temperature field to distort continuously with increasing β_m and Gr^*, compared to the silicon case with low Prandtl number ($\approx 0{\cdot}01$) where the temperature field mimics the conduction limit until high values of the Grashof number ($Gr^* > 10^6$). As the flow intensifies, convection becomes increasingly important for heat transfer through the melt, and the results in Figures 18(c) and 18(d) for $\beta_m = 2{\cdot}7 \times 10^{-7}\ K^{-1}$ ($Gr^* = 3{\cdot}6 \times 10^4$) and $\beta_m = 2{\cdot}7 \times 10^{-5}\ K^{-1}$ ($Gr^* = 1{\cdot}8 \times 10^6$) show the temperature field tracking the streamlines. The melt/crystal interface deflects downward along the centreline as fluid is swept across it by the buoyant recirculation. An indication of the increase of heat transfer from the hot crucible wall to the crystal is evidenced by the decrease in heater temperature needed to maintain the desired crystal radius as β_m increases. This effect is documented in Figure 9(b), where the heater temperature T_H is plotted as a function of the Peclet number for heat transfer in the melt, Pe^*. The data for the GGG calculations are shown as solid circles.

As the intensity of convection increases, the streamlines along the bottom of the vortex begin to undulate (see Figures 18(c) and 18(d)). This pattern evolves since the bottom of the crucible loses heat to the pedestal, and a vertical temperature gradient with colder fluid on the bottom results. The corresponding vertical density profile is stabilizing. Warm fluid in the recirculation which plunges down the centreline of the crucible is retarded by this stabilizing density gradient, producing a stationary pattern which is similar to the formation of lee waves in a stratified fluid.[42] The effects of this density stratification are more pronounced for $\beta = 2{\cdot}7 \times 10^{-5}\ K^{-1}$ ($Gr^* = 1{\cdot}8 \times 10^6$), where a secondary vortex near the lower centreline of the flow domain in nested within

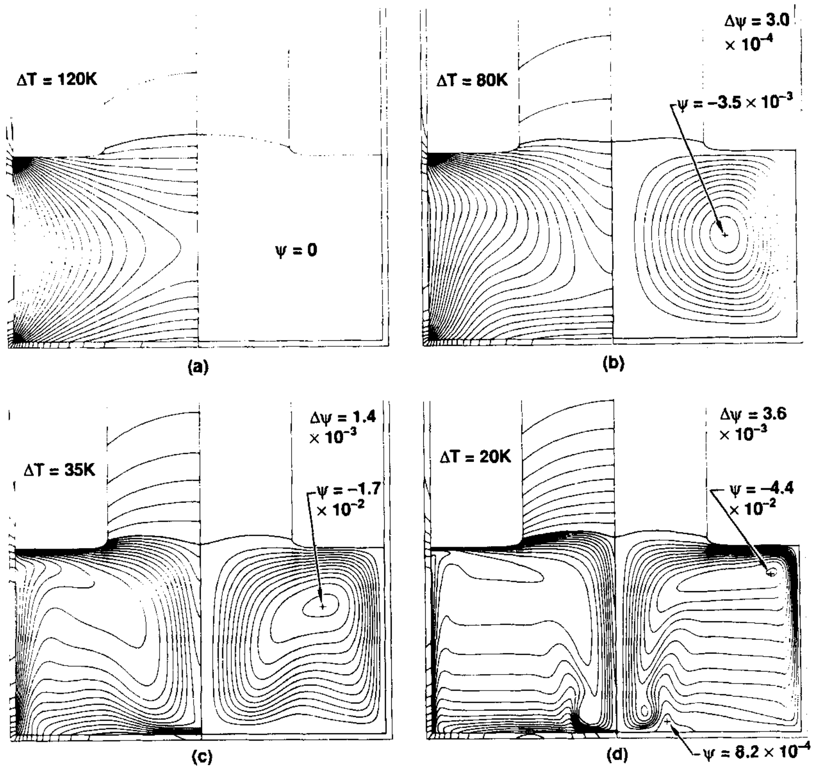

Figure 18. Streamlines, temperature and interface shapes for increasing buoyant convection, HTCM GGG simulation. Isotherm and streamline spacing denoted on plots. (a) $\beta_m = 0\ K^{-1}$, $Gr^* = 0$, $Re^* = 0$, $Pe^* = 0$, $T_H = 4831\ K$. (b) $\beta_m = 2{\cdot}7 \times 10^{-9}\ K^{-1}$, $Gr^* = 9{\cdot}6 \times 10^2$, $Re^* = 6{\cdot}1$, $Pe^* = 28$, $T_H = 3926\ K$. (c) $\beta_m = 2{\cdot}7 \times 10^{-7}\ K^{-1}$, $Gr^* = 3{\cdot}6 \times 10^4$, $Re^* = 97$, $Pe^* = 4{\cdot}5 \times 10^2$, $T_H = 2782\ K$. (d) $\beta_m = 2{\cdot}7 \times 10^{-5}\ K^{-1}$, $Gr^* = 1{\cdot}8 \times 10^6$, $Re^* = 8{\cdot}4 \times 10^2$, $Pe^* = 3{\cdot}9 \times 10^3$, $T_H = 2412\ K$

the primary circulation and a separate, counter-rotating vortex has developed along the crucible bottom. Unlike the appearance of separated flow along the crucible sidewall for Si growth, the formation of recirculation on the crucible bottom probably does not signal a transition to time-periodic flows. In fact, axisymmetric flows qualitatively similar to these were found to be steady by Müller *et al.*[43] in experiments using water ($Pr = 7$). The final calculation in Figure 18(d) for $\beta_m = 2{\cdot}7 \times 10^{-5}\ K^{-1}$ represents the estimated experimental value of the thermal expansion coefficient for GGG.[44]

Contours of radial velocity, axial velocity and pressure are shown as a function of increasing β_m and Gr^* in Figure 19. The velocity contours clearly show the evolution from a simple toroidal roll cell for $\beta_m = 2{\cdot}7 \times 10^{-9}$ ($Gr^* = 960$) to the complicated, multiple-cell flow structure for $\beta = 2{\cdot}7 \times 10^{-5}\ K^{-1}$($Gr^* = 1{\cdot}8 \times 10^6$). Small aphysical wiggles are present in the velocity field for the most highly convected flow field (Figure 19(c)); these wiggles signal the breakdown of the Galerkin formulation for this discretization and will be discussed further in the following section. The pressure field for each calculation is predominantly hydrostatic, caused by the interaction of the Boussinesq term in the momentum equation (4) with the large vertical temperature gradient in the melt. The pressure field near the corners of the flow domain reflects the turning nature of the flow; these effects are crowded closer to the boundaries as the flow intensifies.

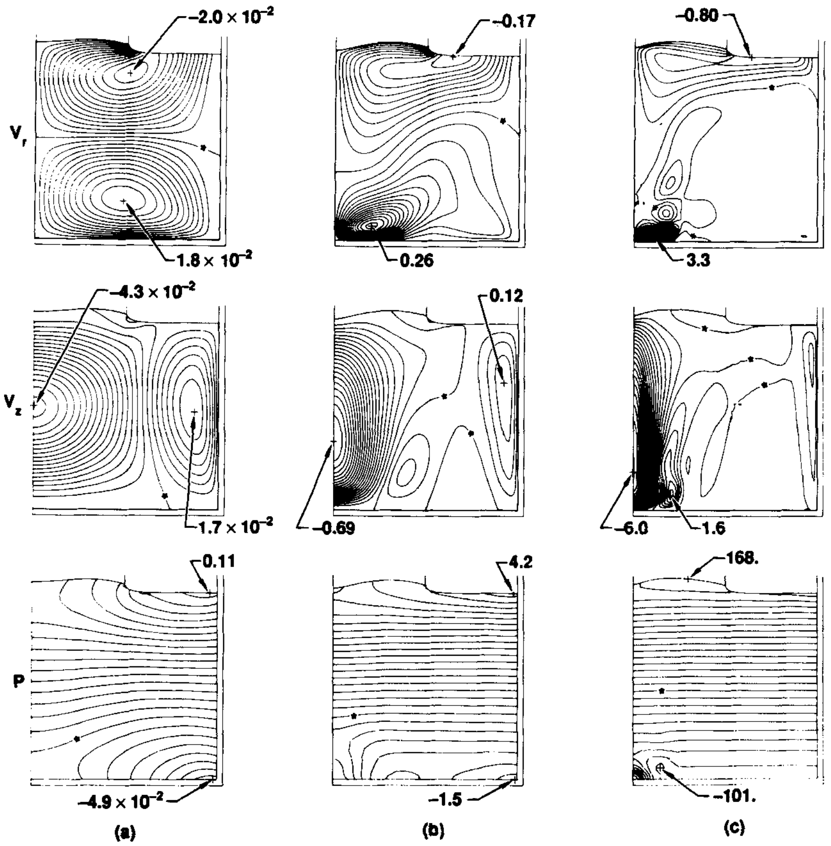

Figure 19. Contours of v_r, v_z, and P for increasing β_m, HTCM GGG simulation. Velocities are in units of cm s^{-1}; pressure is in units of dyne cm^{-2}. Zero contours marked by*. (a) $\beta_m = 2{\cdot}7 \times 10^{-9}\ K^{-1}$, $Gr^* = 9{\cdot}6 \times 10^2$, $\Delta v_r = 1{\cdot}5 \times 10^{-3}$, $\Delta v_z = 2{\cdot}5 \times 10^{-3}$, $\Delta P = 6{\cdot}48 \times 10^{-3}$. (b) $\beta_m = 2{\cdot}7 \times 10^{-7}\ K^{-1}$, $Gr^* = 3{\cdot}6 \times 10^4$, $\Delta v_r = 1{\cdot}7 \times 10^{-2}$, $\Delta v_z = 3{\cdot}3 \times 10^{-2}$, $\Delta P = 0{\cdot}23$. (c) $\beta_m = 2{\cdot}7 \times 10^{-5}\ K^{-1}$, $Gr^* = 1{\cdot}8 \times 10^6$, $\Delta v_r = 0{\cdot}16$, $\Delta v_z = 0{\cdot}3$, $\Delta P = 10{\cdot}8$

Momentum and temperature boundary layers begin forming on the crucible sidewall at relatively low values of β_m and Gr^*. Profiles of the temperature and axial velocity near the crucible sidewall are shown in Figure 20 for several values of Gr^*. In Figures 20(a) and 20(b) the temperature and velocity at $z \approx 0{\cdot}48$, an axial position nearly midway between the crucible bottom and the melt surface, are plotted as functions of the distance from the crucible wall. Boundary layers which decrease in thickness with increasing Grashof number are apparent in both components. The temperature difference between the wall and the bulk decreases as Gr^* increases; this effect is caused by the corresponding decrease in heater temperature as convection increases, as discussed above (see Figure 9(b)). The opposite trend is seen for the axial velocity, which increases with the Grashof number. The temperature and velocity are plotted in terms of scaled quantities in Figures 20(c) and 20(d). In both figures the distance from the wall is plotted in stretched co-ordinates by the appropriate scaling for free convection along a vertical heated plate[45] or for flow in a rectangular cavity.[46] As shown in the figures, for $Gr^* > 10^4$ the boundary layer thickness of both temperature and velocity scales with $[Gr^*Pr]^{1/4}$. However, the magnitude of the axial velocity in the boundary layer does not scale as well with the factor $[Gr^*Pr]^{-1/2}$

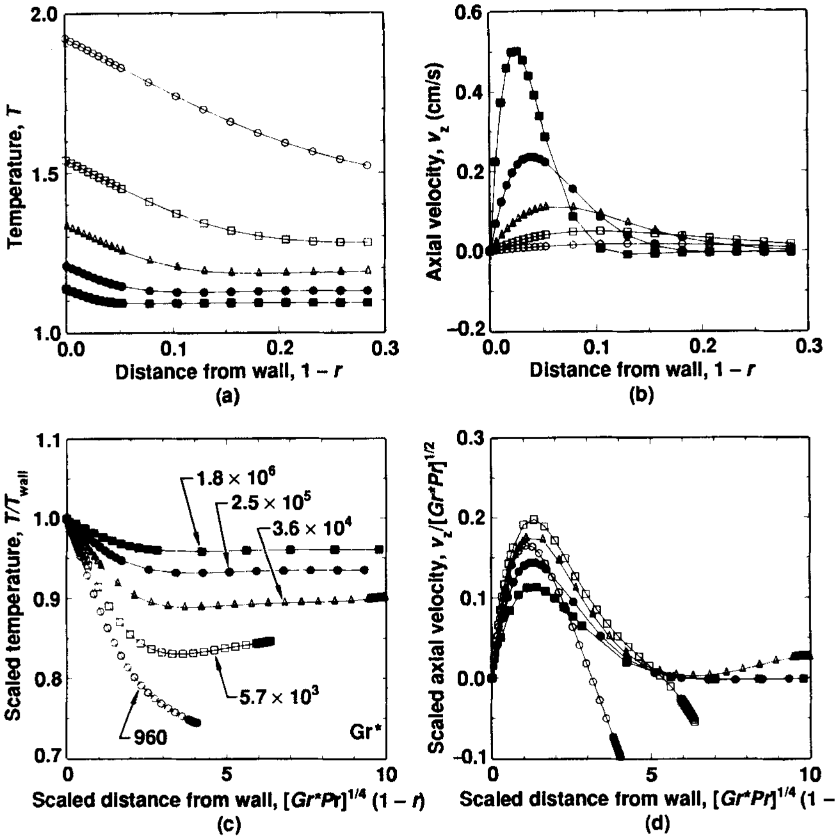

Figure 20. Temperature and axial velocity profiles plotted with increasing distance from crucible wall at $z \approx 0{\cdot}48$

predicted in Reference 46. This lack of agreement may be caused by the impact of the stratified density regime on the flow at higher values of Gr^*.

The effective Reynolds number Re^* is shown as a function of the Grashof number Gr^* for the GGG calculations by the solid circles in Figure 9(a). For values of $Gr^* > 10^4$ the effective Reynolds number increases with $Gr^{*1/2}$. For the $Gr^* = 1{\cdot}8\times10^6$ calculation shown in Figure 18(d), the structure of the primary flow approaches the boundary layer regime discussed by Gill,[46] where the streamfunction and temperature are functions only of axial position in the core, i.e. $\psi \sim \psi(z)$ and $T \sim T(z)$.

The behaviour of the local velocity and pressure field near the tri-junction is examined in Figure 21, where the components of the finite element solution are plotted along a vertical ray emanating from the tri-junction. The data for this plot were taken from the calculation for $\beta_m = 2{\cdot}7\times10^{-5}$ ($Gr^* = 1{\cdot}8\times10^6$) with the finest mesh N3 (see Figure 5(c)). For this simulation the growth angle for GGG was taken to be 17° and the melt/crystal interface was inclined $\approx 23{\cdot}5°$ upward from the horizontal, yielding a total angle of $\phi_T = 130{\cdot}5°$. The Moffatt exponent is calculated to be $\lambda = 1{\cdot}97$ for this angle, and the velocity components should scale as v_ρ, $v_\vartheta \sim r^{\lambda-1} \approx r^1$. The log–log plot 21(b) shows that v_ρ does indeed follow the leading-order behaviour predicted by Moffatt's analysis[27]; however, the other component of velocity, v_ϑ, deviates slightly from the predicted scaling.

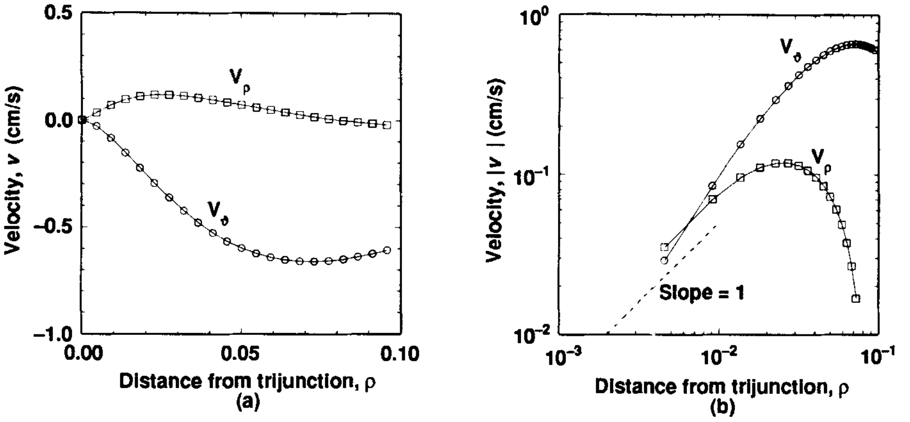

(a) (b)

Figure 21. Velocity field in the vicinity of the tri-junction, plotted along the vertical line at $r=R$. Following this ray to the tri-junction, $\rho \equiv H_1(R,z)-z$, $v_\rho \equiv v_r$, $v_\vartheta \equiv v_z$

5.2. *Assessment of accuracy*

The three meshes shown in Figure 5 were used to examine the accuracy of the results for the high-Prandtl-number calculations. Calculations were performed for $\beta_m = 2{\cdot}7 \times 10^{-5}$ for each mesh, and contours of the solutions are shown in Figures 22–26. The convergence of the results toward the flow structure shown for the finest mesh is apparent, as is the under-resolution of the thermal boundary layers and components of the velocity field by the coarsest mesh in Figures 22(a), 24(a) and 25(a).

Quantitative predictions of the value of Gr^*, the deflection of the melt/crystal interface between the centreline and the crystal edge, the temperature difference across the melt and the maximum pressure difference in the system are listed in Table V for the three meshes. Each of these values converges with mesh refinement. The interface deflection appears to be the most inaccurate of the values tabulated, but the difference $|\Delta H_0|$ is small relative to the maximum deflection that occurs along the middle of the crystal. The shape of the melt/crystal interface depends on the local temperature field, which is expected to be more sensitive to any approximation errors in the velocity field for the high-Prandtl-number oxide melt than for the low-Prandtl-number silicon melt, where conduction heat transport is more dominant. Other values have changed by less than 1% between the two finest meshes N2 and N3.

A measure of the mass conservation by the finite element method for these supposedly divergence-free incompressible flows is shown in Figure 27 by plotting contours of the discrete value of $(\nabla \cdot \mathbf{v})$ for the solutions given by meshes N1, N2 and N3. In each figure, contours of $+0{\cdot}1$ and $-0{\cdot}1$ are plotted; the maximum values of $(\nabla \cdot \mathbf{v})$ are $O(10)$ for each calculation. Pointwise mass conservation improves as the discretization is increased, as is indicated by the larger portions of the flow domain where no contours appear. In addition, the poorest resolution of divergence-free flow by the finite element solutions is seen to occur near discontinuities in the boundary conditions, i.e. in the corners and near the tri-junction, and in areas where the flow structure is complex, i.e. near the bottom centreline of the domain.

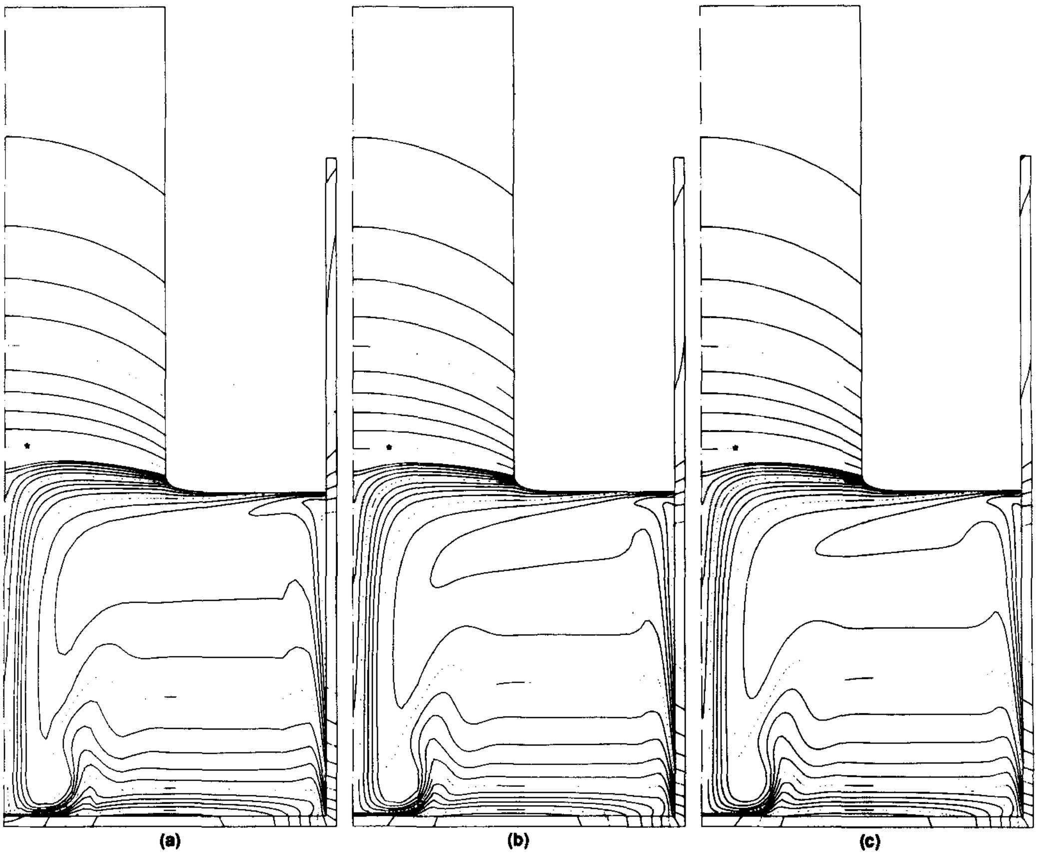
(a) (b) (c)

Figure 22. Temperature contours for HTCM GGG simulation for $\beta_m = 2{\cdot}7 \times 10^{-5}$ K^{-1} ($Gr^* = 1{\cdot}8 \times 10^6$). The isotherms are spaced at 20 K; the contour for 2000 K is marked by*. Meshes: (a) N1, (b) N2, (c) N3

6. DISCUSSION

The Galerkin finite element approximation of the velocity, pressure and temperature fields combined with Newton's method for simultaneous iteration for the interface shapes and field variables is a robust method for solution of the steady state, hydrodynamic thermal-capillary model (HTCM) of CZ growth. With fine finite element discretizations, accurate solutions are obtained with realistic values of the thermophysical properties using only a few (four to six) Newton iterations.

Complex flow structures are predicted for realistic values of the thermophysical parameters for both semiconductor and oxide materials. For the low–Prandtl–number system (Si) the evolution from a viscous-dominated flow to the development of momentum boundary layers with a highly advective core region and finally to thermal boundary layers is observed. Flow separation occurs along the sidewall of the crucible at moderate values of the Grashof number. For idealized models of Czochralski bulk flow, time-dependent calculations[9, 38] and computer-implemented tracking of Hopf bifurcation points[47] have confirmed that time-periodic, axisymmetric motions start after the

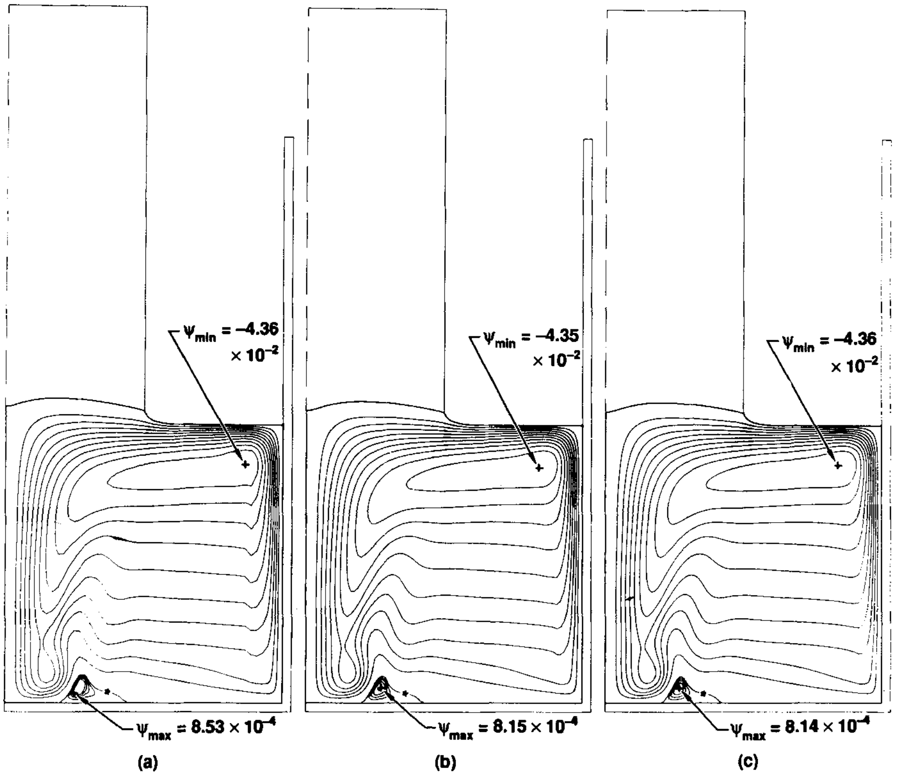

Figure 23. Streamfunction contours for HTCM GGG simulation for $\beta_m = 2{\cdot}7 \times 10^{-5}$ K^{-1} ($Gr^* = 1{\cdot}8 \times 10^6$). The contour spacing is 4×10^{-3} for $\psi < 0$ and 2×10^{-4} for $\psi > 0$; the contour for $\psi = 0$ is marked by*. Meshes: (a) N1, (b) N2, (c) N3

appearance of flow separation. Even the steady state, separated flows are extremely difficult to compute. Our examination of the accuracy of the calculations with mesh refinement for $Gr^* \approx 7 \times 10^6$ shows that accurate prediction of the separated flow requires high resolution of the flow near the solid boundaries and a fine finite element mesh. The meshes used in this study are more resolved than those used in the time-dependent calculations and are comparable to those used in Reference 47 for detection of Hopf bifurcation points. Moreover, Winters *et al.*[47] demonstrate that inaccurate resolution of the flow overestimates the value of Gr^* for the onset of time-periodic motion, as is expected because of the extra viscous dissipation implied by the inadequate representation of thin boundary layers on a coarse mesh.

Flow structure for the high–Prandtl–number system (GGG) evolves in a markedly different manner than for the low–Prandtl–number semiconductor system. For even moderate Grashof numbers ($Gr^* = O(10^4)$), boundary layer structure is clearly evident in the temperature field of the melt. The temperature and velocity field near the crucible wall scale according to boundary layer flow along a heated vertical surface. Unlike the semiconductor melt, separation of the sidewall boundary layer does not occur as the flow intensifies, but a secondary vortex and an additional counter-rotating vortex form at the bottom of the crucible near the centreline at $Gr^* = 2 \times 10^6$. There is some evidence that the axisymmetric flows calculated for this realistic value of the

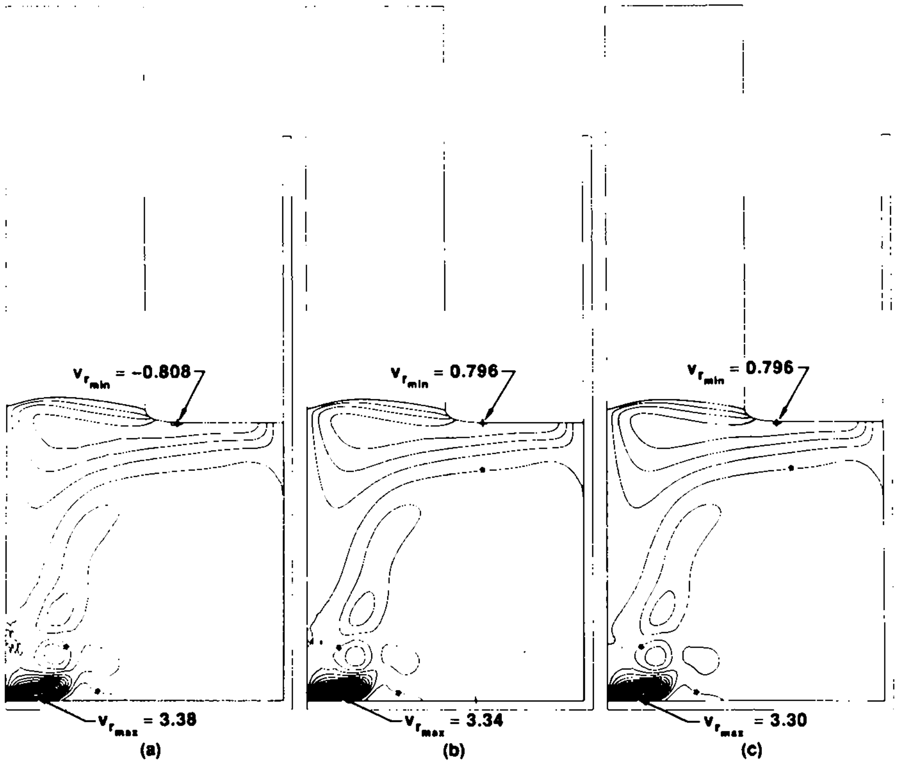

Figure 24. Radial velocity contours for HTCM GGG simulation for $\beta_m = 2{\cdot}7 \times 10^{-5}$ K^{-1} ($Gr^* = 1{\cdot}8 \times 10^6$). The contour spacing is 0·2 cm s^{-1}; the contour for 0 cm s^{-1} is marked by*. Meshes: (a) N1, (b) N2, (c) N3

Grashof number are stable, as shown by the experimental results of Müller *et al.*[43] and the bulk flow calculations of Langlois.[44] The cooling of the bottom of the crucible in these simulations has a stabilizing effect on the flow; calculations in Reference 29 address the effect of changing the heat transfer from the crucible bottom.

Including the other driving forces for convection, crucible and crystal rotation and surface-tension-driven motions will make the flow structure even more complicated. Internal shear layers will form because of competition between flows driven by several sources; the evolution of such flows will be addressed in another paper. Accurate approximation of internal layers require highly resolved calculations in the interior of the flow domain as well as near the boundaries of the melt domain. Meshes at least as fine as those used here are needed to resolve these layers, especially if the onset of time-dependent flows is to be predicted accurately.

The agreement between the finite element predictions for the velocity field near the melt/crystal/ambient tri-junction and the asymptotic analysis which is valid in the limit of $Ca \rightarrow 0$ is evidence that the behaviour of the flow near this singularity is not destroying the accuracy of the finite element method elsewhere. Interestingly, the flow near the tri-junction is more easily approximated for the realistic growth angles ϕ_0 used in this analysis, which are appropriate for crystal growth systems, than for the value $\phi_0 = 90°$ used before in the idealized bulk flow calculations. The pressure and stress are not as singular for small values of ϕ_0 as they are for the flat meniscus case.

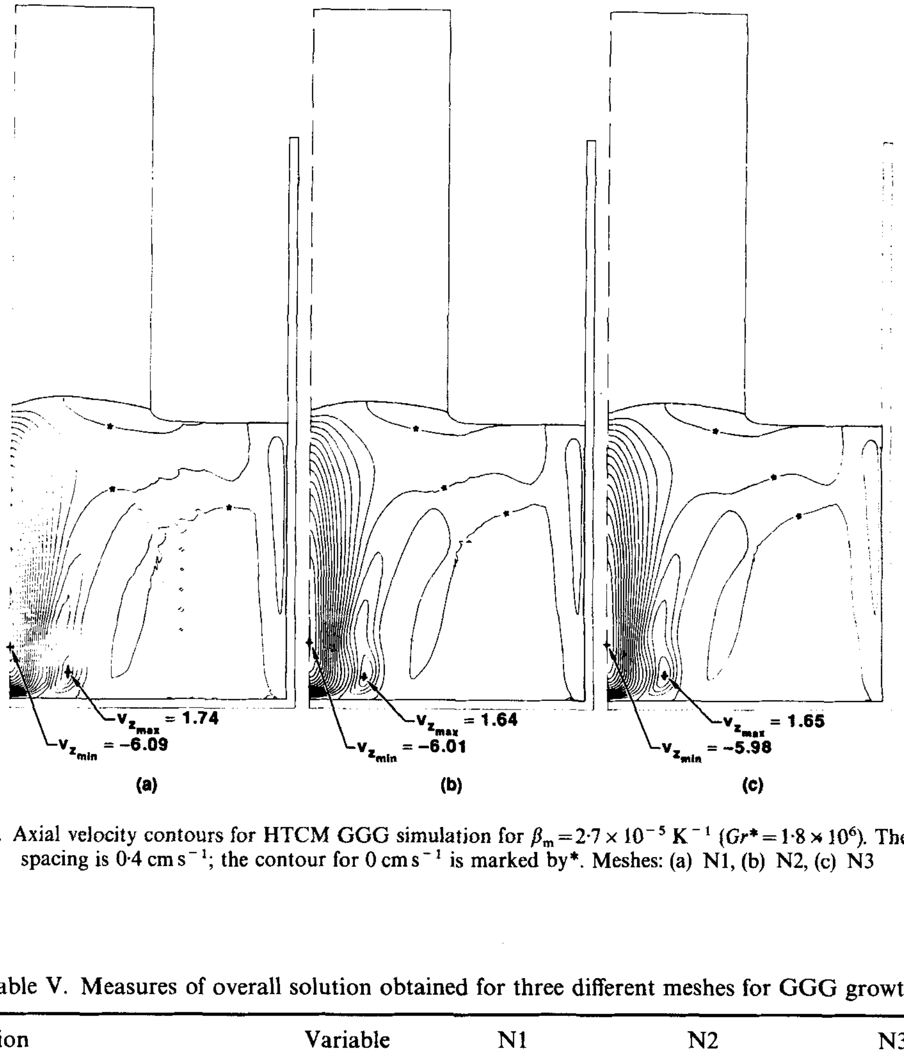

Figure 25. Axial velocity contours for HTCM GGG simulation for $\beta_m = 2{\cdot}7 \times 10^{-5}$ K^{-1} ($Gr^* = 1{\cdot}8 \times 10^6$). The contour spacing is 0·4 cm s^{-1}; the contour for 0 cm s^{-1} is marked by*. Meshes: (a) N1, (b) N2, (c) N3

Table V. Measures of overall solution obtained for three different meshes for GGG growth

Description	Variable	N1	N2	N3
No. of radial elements in melt	NE_{mr}	23	38	47
No. of axial elements in melt	NE_{mz}	23	35	45
No. of velocity unknowns in melt	N_v	6627	16401	25935
No. of pressure unknowns in melt	N_p	1587	3990	6345
Total no. of unknowns	N_{tot}	12042	28419	44079
CPU sec/Newton iteration		40	190	360
Streamfunction minimum	ψ_{min}	$-4{\cdot}359 \times 10^{-2}$	$-4{\cdot}354 \times 10^{-2}$	$-4{\cdot}358 \times 10^{-2}$
Streamfunction maximum	ψ_{max}	$8{\cdot}532 \times 10^{-4}$	$8{\cdot}154 \times 10^{-4}$	$8{\cdot}143 \times 10^{-4}$
Temperature difference across melt domain	ΔT_{melt}	0·17852	0·17522	0·17434
Heater temperature	T_H	1·1985	1·1923	1·1907
Melt/crystal interface deflection	$\lvert\Delta H_0\rvert$	−0·01404	−0·00607	−0·00381
Grashof no.	Gr^*	$1{\cdot}852 \times 10^6$	$1{\cdot}817 \times 10^6$	$1{\cdot}808 \times 10^6$
Reynolds no.	Re^*	853·8	842·4	839·2
Range of pressure	ΔP	277·0	265·3	263·5

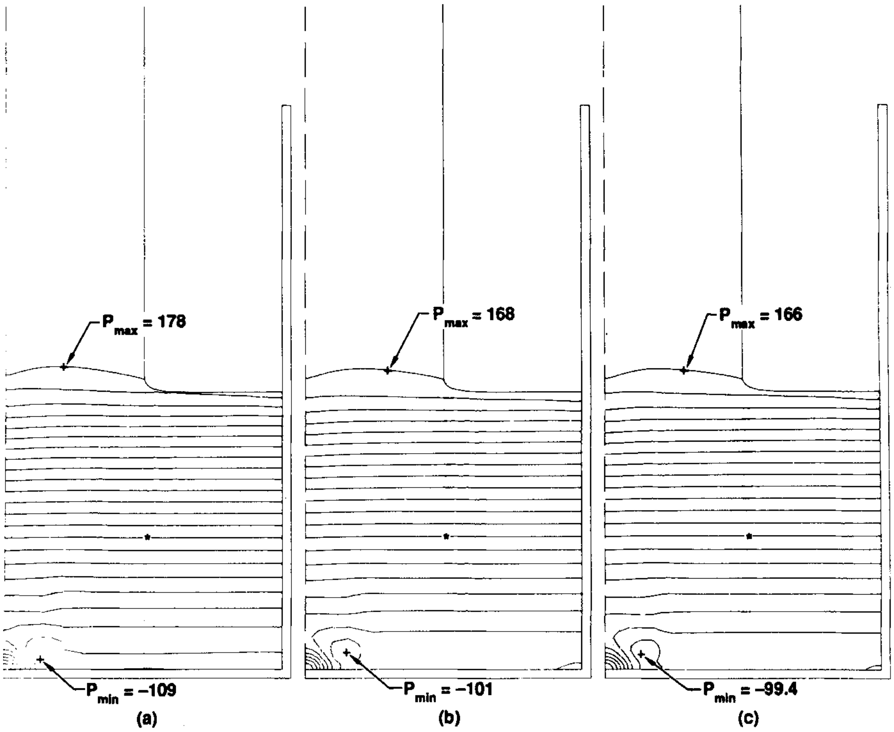

(a) (b) (c)

Figure 26. Pressure contours for HTCM GGG simulation for $\beta_m = 2{\cdot}7 \times 10^{-5}$ K^{-1} ($Gr^* = 1{\cdot}8 \times 10^6$). The contour spacing is 13·96 dyne cm^{-2}; the contour for 0 dyne cm^{-2} is marked by*. Meshes: (a) N1, (b) N2, (c) N3

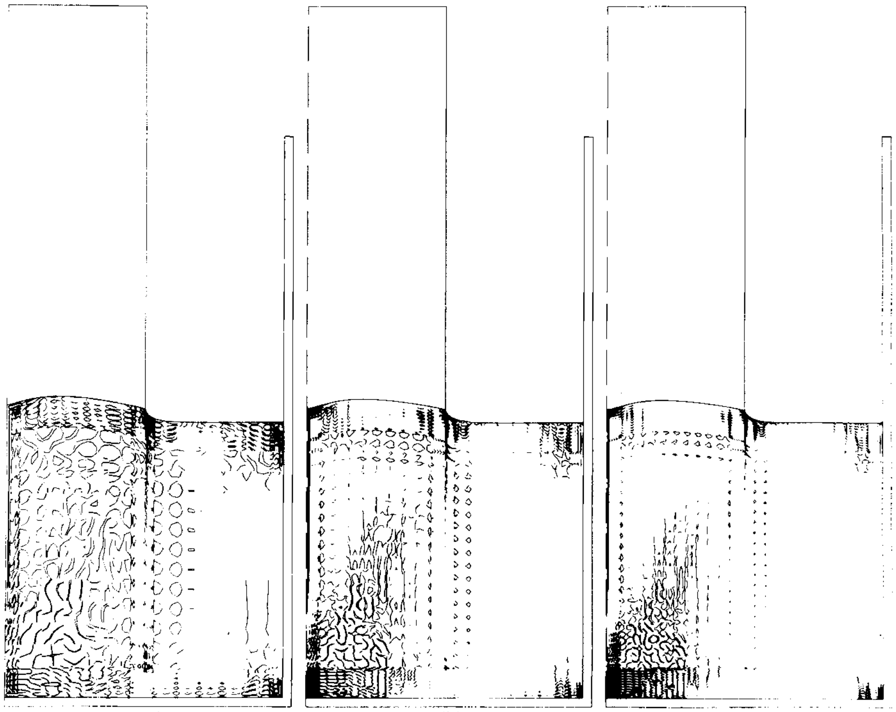

(a) (b) (c)

Figure 27. Contours for discrete values for $(\nabla \cdot \mathbf{v}) = \pm 0{\cdot}1$ for HTCM GGG simulation for $\beta_m = 2{\cdot}7 \times 10^{-5}$ K^{-1} ($Gr^* = 1{\cdot}8 \times 10^6$). Meshes: (a) N1, (b) N2, (c) N3

ACKNOWLEDGEMENTS

Computational resources were supplied by the Pittsburgh Scientific Computing Center through a grant from the Office of Advanced Scientific Computing of the National Science Foundation. P. M. Gresho of LLNL provided invaluable insight during the development of this model. This work was performed under the auspices of the U.S. Department of Energy by Lawrence Livermore National Laboratory under Contract W-7405-Eng-48 and by the Defense Advanced Research Projects Agency.

REFERENCES

1. R. A. Brown, 'Theory of transport processes in single crystal growth from the melt: a review', *AIChE J.*, **34**, 881–911 (1988).
2. W. Zulehner, 'Czochralski growth of slicon', *J. Crystal Growth*, **65**, 189–213 (1983).
3. D. T. J. Hurle, 'The evolution and modelling of the Czochralski growth technique', *J. Crystal Growth*, **85**, 1–8 (1987).
4. C. D. Brandle, 'Crystal pulling', in B. R. Pamplin (ed.), *Crystal Growth*, 2nd Edn, Pergamon Press, Oxford, 1980.
5. L. M. Foster, 'The preparation of III–V semiconductor alloys', in W. R. Wilcox and R. A. Lefever (eds.), *Preparation and Properties of Solid State Materials, Vol. 3*, Marcel Dekker, New York, 1977.
6. W. E. Langlois, 'Buoyancy-driven flows in crystal-growth melts', *Ann. Rev. Fluid Mech.*, **17**, 191–215 (1985).
7. N. Kobayashi, 'Heat transfer in Czochralski crystal growth', in W. R. Wilcox (ed.), *Preparation and Properties of Solid State Materials, Vol. 6*, Marcel Dekker, New York, 1981, pp. 119–253.
8. M. Mihelčic, C. Scröck-Pauli, K. Wingerath, H. Wenzl, W. Uelhoff and A. van der Hart, 'Numerical simulation of free and forced convection in the classical Czochralski method and in CACRT', *J. Crystal Growth*, **57**, 300–317 (1982).
9. M. J. Crochet, P. J. Wouters, F. T. Geyling and A. S. Jordan, 'Finite-element simulation of Czochralski bulk flow', *J. Crystal Growth*, **65**, 153–165 (1983).
10. M. Mihelčic, K. Wingerath and Chr. Pirron, 'Three-dimensional simulations of the Czochralski bulk flow', *J. Crystal Growth*, **69**, 473–488 (1984).
11. A. B. Crowley, 'Mathematical modelling of heat flow in Czochralski crystal pulling', *IMA J. Appl. Math.*, **30**, 173–189 (1983).
12. J. J. Derby, R. A. Brown, F. T. Geyling, A. S. Jordan and G. A. Nikolakopoulou, 'Finite element analysis of a thermal-capillary model for liquid encapsulated Czochralski growth', *J. Electrochem. Soc.*, **132**, 470–482 (1985).
13. R. K. Srivastava, P. A. Ramachandran and M. P. Dudukovic, 'Interface shape in Czochralski grown crystals: effect of conduction and radiation', *J. Crystal Growth*, **73**, 487–504 (1985).
14. L. J. Atherton, J. J. Derby and R. A. Brown, 'Radiative heat exchange in Czochralski crystal growth', *J. Crystal Growth*, **84**, 57–78 (1987).
15. J. J. Derby, 'Analysis of heat transfer, stability, and dynamics of Czochralski and liquid encapsulated Czochralski growth of semiconductor materials', *Ph.D. Thesis*, Massachusetts Institute of Technology (1986).
16. W. J. Silliman and L. E. Scriven, 'Separation flow near a static contact line: slip at a wall and shape of a free surface', *J. Comput Phys.*, **34**, 287 (1980).
17. S. F. Kistler and L. E. Scriven, 'Coating flow theory by finite element and asymptotic analysis of the Navier–Stokes system', *Int. j. numer. methods fluids*, **4**, 207–229 (1984).
18. J. Bemelmans, in P. Concus and R. Finn (eds), *Variational Methods for Free Surface Interfaces*, Springer-Verlag, New York, 1987.
19. H. M. Ettouney and R. A. Brown, 'Finite-element methods for steady solidification problem', *J. Comput Phys.*, **49**, 118–150 (1983).
20. C. J. Chang and R. A. Brown, 'Natural convection in steady solidification finite element analysis of a two-phase Rayleigh–Bénard problem', *J. Comput. Phys.*, **53**, 1–27 (1984).
21. P. M. Adornato and R. A. Brown, 'Petrov–Galerkin methods for natural convection in directional solidification of binary alloys', *Int. j. numer. methods fluids*, **7**, 761–791 (1987).
22. K. J. Ruschak, 'A method for incorporating free boundaries with surface tension in finite element fluid-flow simulators', *Int. j. numer. methods fluids*, **15**, 639–648 (1980).
23. H. Saito, and L. E. Scriven, 'Study of coating flow by the finite element method', *J. Comput. Phys.*, **42**, 53–76 (1981).
24. M. J. Crochet, F. T. Geyling and J. J. Van Schaftigen, 'Numerical simulation of the horizontal Bridgman growth. Part I: Two-dimensional flow', *Int. j. numer. methods fluids*, **7**, 29–48 (1987).
25. E. B. Dussan V, 'On the spreading of liquids on solid surfaces: static and dynamic contact lines', *Ann. Rev. Fluid Mech.*, **11**, 371–400 (1979).
26. W. R. Dean and P. E. Montagnon, 'On the steady motion of viscous liquid in a corner', *Proc. Camb. Phil. Soc.*, **45**, 389 (1949).
27. H. K. Moffatt, 'Viscous and resistive eddies near a sharp corner', *J. Fluid Mech.*, **18**, 1–18 (1964).
28. S. A. Trogdon and D. D. Joseph, 'The stick-slip problem for a round jet I. Large surface tension', *Rheol. Acta*, **19**, 404–420 (1980).

29. J. J. Derby, L. J. Atherton and P. M. Gresho, 'An integrated process model for the growth of oxide crystals by the Czochralski method', *J. Crystal Growth*, submitted (1988).
30. J. J. Derby and R. A. Brown, 'On the quasi-steady-state assumption in modeling Czochralski crystal growth', *J. Crystal Growth*, **87**, 251–260 (1987).
31. P. M. Gresho and J. J. Derby, 'A finite element model for induction heating of a metal crucible', *J. Crystal Growth*, **85**, 40–48 (1987).
32. J. J. Derby and R. A. Brown, 'Thermal-capillary analysis of Czochralski and liquid encapsulated C Czochralski crystal growth II. Processing strategies', *J. Crystal Growth*, **75**, 227–240 (1986).
33. G. Strang and G. J. Fix, *An Analysis of the Finite Element Method*, Prentice–Hall, Englewood Cliffs, New Jersey, 1973.
34. R. L. Sani, P. M. Gresho, R. L. Lee and D. F. Griffiths, 'The cause and cure (?) of the spurious pressures generated by certain FEM solutions of the incompressible Navier–Stokes equations: Part 1, *Int. j. numer. methods fluids*, **1**, 17–43 (1981).
35. J. J. Derby, L. J. Atherton, P. D. Thomas and R. A. Brown, 'Finite element methods for analysis of the dynamics and control of Czochralski crystal growth', *J. Sci. Comput.*, **2**, 297–343 (1987).
36. P. Hood, 'Frontal solution program for unsymmetric matrices,' *Int. j. numer. methods eng.*, **10**, 379–399 (1976).
37. Y. Yamaguchi, C. J. Chang, and R. A. Brown, 'Multiple buoyancy-driven flows in a vertical cylinder heated from below', *Phil. Trans. R. Soc. London A*, **312**, 519–552 (1984).
38. A. Bottaro and A. Zebib, 'Bifurcation in axisymmetric Czochralski natural convection', *Phys. Fluids*, **31**, 495–501 (1988).
39. W. E. Langlois and K. Lee, 'Digital simulation of magnetic Czochralski flow under various laboratory conditions for silicon growth', *IBM J. Res. Devlop.*, **27**(3), 281–284 (1983).
40. A. Acrivos, 'On the combined effect of forced and free convection heat transfer in laminar boundary layer flows', *Chem. Eng. Sci.*, **21**, 343–352 (1966).
41. P. M. Gresho and R. L. Lee, 'Don't suppress the wiggles—they're telling you something!' *Comput. Fluids*, **9**, 223–253 (1981).
42. J. S. Turner, *Buoyancy Effects in Fluids*, Cambridge University Press, London, 1973.
43. G. Müller, G. Neumann and H. Matz, 'A two-Rayleigh-number model of buoyancy-driven convection in vertical melt growth configurations', *J. Crystal Growth*, **84**, 36–49 (1987).
44. W. E. Langlois, 'Effect of the buoyancy parameter on Czochralski bulk flow in garnet growth', *J. Crystal Growth*, **46**, 743–746 (1979).
45. H. Schlichting, *Boundary-layer Theory*, 7th Edn, McGraw-Hill, New York, 1979.
46. A. E. Gill, 'The boundary-layer regime for convection in a rectangular cavity', *J. Fluid Mech.*, **26**(3), 515–536 (1966).
47. K. H. Winters, K. A. Cliff and C. P. Jackson, in R. W. Lewis, (ed), *Numerical Methods in Transient and Coupled Problems*, Wiley, 1987.